# Adaptive Generalized-Minimum-Variance Attitude Control of a High Pointing-Accuracy Remote Sensing Satellite

**Ali Kasiri[1]** , **Farhad Fani Saberi[2]\*** and **Vahid Joudakian[3]**

1. Ph.D. Student, Department of Aerospace Engineering, Amirkabir University of Technology, Tehran, Iran
2. Assistant Professor, Space Science and Technology Institute, Amirkabir University of Technology, Tehran, Iran
3. M.Sc. Student, Department of Electrical Engineering, Amirkabir University of Technology, Tehran, Iran

**\*Corresponding Author's E-mail: f.sabery@aut.ac.ir**

*Abstract*

*Many studies have investigated the problem of external disturbance rejection and also increasing the attitude control system's robustness against the parametric uncertainties. Due to stochastic properties, noise effect minimization becomes an interesting and challenging problem in the field of spacecraft attitude control that has been underestimated, while control actuators and attitude sensors themselves are important sources of noise generation. Therefore, the main purpose of this paper is to (i)control the satellite's attitude and (ii)minimize the variance of output, simultaneously. The minimum variance controller, which is considered the simplest type of model predictive controller, has a powerful capability for minimizing the effects of output noise. This feature makes it a suitable control scheme for space-based high-resolution photography missions. Thus, we described the conventional minimum variance regulator method at first, then an incremental version of the regulator has been presented to solve the tracking problem. Finally, the generalized minimum variance controller which can control both minimum-phase and non-minimum-phase systems is derived for a high pointing accuracy spacecraft. The simulation results show the efficiency of the proposed controller to restrain the noise effects in a high-resolution tri-stereo imaging mission.*

## Nomenclature

| | | | |
|---|---|---|---|
| $I_w$ | Reaction wheel's moment of inertia | $x$ | mean square (MS) |
| $u$ | Control torque | $\omega_c$ | Corner frequency |
| $\mu$ | Standard gravitational parameter of the Earth | $d$ | Time delay |
| $r_0$ | Satellite orbit radius | $E$ | Expected value |
| $\omega_0$ | Orbital frequency | $e(t)$ | Gaussian white noise |
| $H_B$ | Total angular momentum of the spacecraft | $J$ | Cost function |
| $h_{sat}$ | Angular momentum of the only | $A(q^{-1})$ | Denominator of the discrete-time transfer function |
| | | $B(q^{-1})$ | numerator of the discrete-time transfer function |

| | |
|---|---|
| $C(q^{-1})$ | Noise dynamic polynomial in discrete domain |
| $K$ | KALMAN Gain / Correction gain |
| $X(k)$ | State vectors in the discrete domain |
| $X$ | State vector in the continuous domain |
| $r(t)$ | Reference input |
| $\omega = [\omega_x, \omega_y, \omega_z]^T$ | Angular rate vector of the spacecraft |
| $I = diag(I_x, I_y, I_z)$ | Spacecraft's moment of inertia tensor |
| $T_{Ext} = [T_x, T_y, T_z]^T$ | Total external force vector |
| $T_{GG} = [T_{GG_x}, T_{GG_y}, T_{GG_z}]^T$ | Gravity gradient disturbance torque vector |
| $[\psi, \theta, \phi]$ | Euler angles [psi, theta, phi] |
| $[\psi_0, \theta_0, \phi_0]$ | Initial Euler angles |
| $[\psi_d, \theta_d, \phi_d]$ | Desired Euler angles |
| $h_w = [h_{w_x}, h_{w_y}, h_{w_z}]^T$ | Angular momentum vector of the reaction wheels |
| $h_{sat} = [h_x, h_y, h_z]^T$ | Angular momentum vector of the spacecraft's body |
| $\hat{y}$ | Estimated Output |
| $\Phi$ | Regressors vector |
| $\hat{\theta}$ | Estimated Parameters |
| $P$ | Covariance matrix |
| $\varepsilon$ | Noise Estimator/Observer |
| $G$ | discrete-time state-space matrix |
| $H$ | discrete-time state-space matrix |
| $y(k)$ | Discrete-time system output |
| $u(k)$ | Discrete-time system Input |
| $T_C = [T_{c_x}, T_{c_y}, T_{c_z}]^T$ | Control Input in the continuous domain |
| $WN_{hardware}$ | Parasitic noise of hardware |

## Introduction

Thousands of satellites are now in operation for various purposes such as communication, navigation, mapping, military services, space-based mining, weather forecasting, remote sensing, and astronomical observations. Among these missions, space-based monitoring of the Earth is of particular importance and plays a significant role in the space economy. Thus, a great portion of the Low Earth Orbit (LEO) orbiting satellites are the Earth observation type and it is crystal clear that pointing-accuracy and precession play an important role in the quality level of remote sensing missions. Meanwhile, the acquisition of 3D and topographic images based on satellite imagery has attracted particular attention, recently. Traditionally, stereoscopic measurements could only be achieved by acquiring aerial photographs taken from different viewing angles by balloons, unmanned or manned aircraft. But the launch of the Very-High-Resolution (VHR) sensor satellites has paved the way for space-based/satellite-based stereoscopic measurements. Subsequently, the concept of Tri-Stereo-Satellite-Imagery (TSSI) was also born. The TSSI also called "stereoscopy" or "3D imaging" is a photography technique originally developed for creating the illusion of depth in an image [1-3]. In this regard, three pictures of an object (target area) are taken from slightly different angles allowing for depth to be perceived when viewing the images, as shown in Fig.1. Recently, TSSI based on at least 3-satellites (satellite constellation) has been replaced by a single agile and maneuverable satellite along the same orbit [4,5].
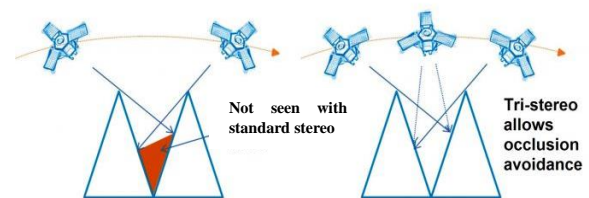


**Fig. 1.** Tri-stereo imagery concept

TSSI is a cost-effective and really useful way to obtain access to the high-precision Digital Elevation Models (DEM), especially over remote and large areas [6,7] such as mountainous and strategic regions of western and northwestern Iran. Fig.2 shows an example of DEM.

The availability of such images has given new possibilities to use satellite images in high detail Geographic Information Systems (GISs), including city planning, farm management, real-estate inventory, and natural risk management. regardless of geographical studies, DEM technic has critical importance in the field of national security.
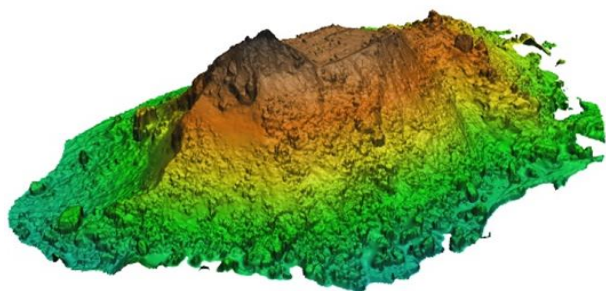
**Fig. 2.** digital elevation model based on TSSI

To process and combine images for achieving a useful 3D image of a specific area, at least 3 satellite-based photos with a resolution of 1 meter and better are needed. Many satellites offer TSSI services such as SPOT-6, EROS_A, IRS, Cartosat1, Dubaisat-2, Deimos-2, Kompsat, Kazeosat, Cartosat-2and IKONOS-1.

According to Table 1, Pointing knowledge, accuracy, and stability of the high-resolution (Hi-Res) remote sensing satellites reach 0.01 deg, 0.1 deg and 0.002 deg∕s, respectively.

High pointing-accuracy, high-precession, and agility are three key requirements of TSSI missions [8,9]. Furthermore, the performance of the attitude control

system plays an important role in the resolution of the photos and accordingly, the quality of the mission [10]. Reaction wheels (RW) are reliable, precise, and cost-effective actuators that provide high pointing-accuracy and can produce a wide range of torque [11]. In comparison with thrusters, the continuous and smooth torque of RWs are more suitable for VHR imaging [12]. As proof, all the mentioned high-resolution remote sensing satellites are using at least 3 reaction wheels in imaging mode. Despite RWs' known advantages, they may suffer from momentum saturation. Due to the lightweight, reliability, simplicity, and low power consumption of the magnetorquers, they are greatly effective in RWs desaturation, especially in LEO [13]. Therefore, it can be claimed that almost all tri-stereo-imagery satellites use both reaction wheels and magnetorquers together [14].

As a further explanation, some TSSI satellites use thrusters or control momentum gyros (CMGs) along with the reaction wheels. In this case, thrusters or CMGs perform maneuverability requirements (doing high-angle and agile maneuvers), and RWs perform pointing-accuracy and precise stability requirements.

Different control actuators' general specifications are presented in Table 1

**Table. 1.** General specifications of RW and thruster

| Actuator | Weight [kg] | Power [w] | Accuracy [deg] | Torque level [Nm] | Minimum number of required |
|---|---|---|---|---|---|
| CMG | > 17 | 30 − 150 | 0.0005 to 0.5 | 25 − 200 | 4 |
| Thruster | 1 − 10 | 1 − 100 (Electrical and HALL effect) | 0.3 − 1.2 | $1\mu N - 10N$ | 6 |
| Reaction wheel | 0.2 − 2 | 0.6 − 10 | 0.001 to 0.2 | 0.01 to 1 | 3 |
| Magnetorquers | 0.05 − 10 | 0.6 − 18 | 5 to 10 | 0.001 to 0.01 | 3 |

The external disturbance torques are cited as a major nuisance for achieving high accuracy and precession in imaging mode [15]. Subsequently, various solutions have been considered to reject them [16-21]. Even, NASA's Disturbance Reduction System (DRS) technology can be mentioned as a practical solution [22,23]. Unfortunately, these methods are not good enough for high-resolution imaging missions. Because, the pointing accuracy and stability of spacecraft are not only affected by external disturbances such as gravity gradient, solar radiation pressure, atmospheric drag, and electromagnetic effects but also onboard disturbances [24,25]. The onboard disturbances (also known as internal disturbances) come in the form of vibrations (periodic signals) and/or transient, and random disturbances. However, minimizing the effect of parasitic noise is a significant

problem, which is not considered in most researches. The point is, although the noise effect may be negligible in comparison with the external disturbances, it cannot be ignored for VHR imagery satellites. Since extremely accurate attitude control is required in a spacecraft whose payloads are observation telescopes that operate in different light spectra. As an example, for space telescopes (Hobble or James Webb) [26,27], attitude stability of several arcsec/sec and pointing accuracy of 0.01 degree (or maybe less) are required. These standards must be achieved despite parasitic disturbances and sensor noise. Noise is relatively harder to deal with in comparison with external disturbances. Space environmental disturbances show relatively harmonic behavior, so they can be modeled and predicted. But noise cannot be predicted due to its "stochastic" nature

and cannot be eliminated completely [28,29]. Moreover, unlike disturbance torques, noise is known as a high-frequency phenomenon (apart from external noise sources such as the sun, atmosphere, etc.). Some onboard components of a satellite such as rate gyros, attitude sensors and reaction/momentum wheels (especially in high RPM) are also important sources of parasitic noise [30]. We have to minimize the effect of these hardware noises to achieve high pointing accuracy and precession in High-resolution imagery missions.

Control of stochastic linear systems with unknown or slow time-varying parameters is of great theoretical interest [31]. There are two main approaches in this field: (i) model-reference, and (ii) self-tuning, which both contributed to the emergence of the adaptive predictive controller. The conventional Minimum Variance (MV) regulator has a powerful tool to reduce the effect of noise [32]. This controller is able to decrease output variance to the minimum possible (white noise variance) [33]. An Incremental Minimum Variance Controller (IMVC) is created to solve the tracking problem. Both MV and IMVC were useful only for minimum-phase systems. Hastings-James and later Clarke [34], modified these control laws by adding a control costing term. Finally, the Generalized Minimum Variance Controller (GMVC) is presented as a complete control algorithm that can control both minimum-phase and non-minimum-phase systems. GMVC was initially formulated for single-input single-output (SISO) systems [35]. Koivo extended this version to the multi-input multi-output (MIMO) case [36]. Through this control approach, a trade-off can be found between minimizing the output error variance and smoothing control variations by selecting suitable weight functions. It is clear that continuous-time controller laws will show a good performance only for a very small sampling-period since it does not take into account the sampling-time in the design procedure. The discrete GMVC considers the sampling period in the design phase and therefore can give better performance, even if the sampling period is considerably large. It is also more suitable for spacecraft onboard computing in practical aspects [37]. Moreover, the controller designed in the discrete domain also has an advantage in terms of implementation.

Due to the uncertainties and changes in the satellite's dynamic parameters during its lifetime, the adaptive-based controller will definitely perform a better performance than time-invariant ones. In summary, minimum variance control is one of the useful approaches that partially covers the whole set of stated benefits. However, no discussion is made about the use

of MVC/GMVC in the field of satellite attitude control so far, despite being of great theoretical and practical interest. So in this paper, we proposed adaptive GMVC as an optimal approach to meet the attitude control requirements of a High-Resolution remote sensing satellite in its imaging phase. This approach uses the recursive least square (RLS) algorithm to update the controller parameters in accordance with the changes in dynamics parameters.

The paper is organized as follows. ADCS different operational modes are introduced in chapter 2. The problem formulation is presented in Chapter 3. In this regard, the dynamical and kinematic models of a rigid spacecraft are expressed in continuous-time. Subsequently, the discretization of the equations is performed and, Section 3 ends with RWs Noise Modeling, finally. The design principles of the controller are discussed in the fourth Section. The simulation results are presented and analyzed in Section 5. The article ends with the conclusion section in Section 6

The external disturbance torques are cited as a major nuisance for achieving high accuracy and precession in imaging mode [15]. Subsequently, various solutions have been considered to reject them [16-21]. For instance, the Disturbance Reduction System (DRS) technology developed by NASA can be mentioned as a practical solution [22,23]. Unfortunately, these methods are not good enough for high-resolution imaging missions. Because, the pointing accuracy and stability of spacecraft are not only affected by external disturbances such as gravity gradient, solar radiation pressure, atmospheric drag, and electromagnetic effects but also onboard disturbances [24,25]. The onboard disturbances (also known as internal disturbances) come in the form of vibrations (periodic signals) and/or transient, and random disturbances. However, minimizing the effect of parasitic noise is a significant problem, which is not considered in most researches. The point is, although the noise effect may be negligible in comparison with the external disturbances, it cannot be ignored for VHR imagery satellites. Since extremely accurate attitude control is required in a spacecraft whose payloads are observation telescopes that operate in different light spectra. As an example, for space telescopes (Hobble or James Webb) [26,27], attitude stability of several arcsec/sec and pointing accuracy of 0.01 degree (or maybe less) are required. These standards must be achieved despite parasitic disturbances and sensor noise. Noise is relatively harder to deal with in comparison with external disturbances. Space environmental disturbances show relatively harmonic behavior, so they can be modeled and

predicted. But noise cannot be predicted due to its "stochastic" nature and cannot be eliminated completely [28,29]. Also, unlike disturbance torques, noise is known as a high-frequency phenomenon (apart from external noise sources such as the sun, atmosphere, etc.). Some onboard components of a satellite such as rate gyros, attitude sensors and reaction/momentum wheels (especially in high RPM) are also important sources of parasitic noise [30]. We have to minimize the effect of these hardware noises to achieve high pointing accuracy and precession in Hi-Res imagery missions.

Control of stochastic linear systems with unknown or slow time-varying parameters is of great theoretical interest [31]. There are two main approaches in this field, (i) model-reference, and (ii) self-tuning, which both contributed to the emergence of the adaptive predictive controller. The conventional Minimum Variance (MV) regulator has a powerful tool to reduce the effect of noise [32]. This controller is able to decrease output variance to the minimum possible (white noise variance) [33]. An Incremental Minimum Variance Controller (IMVC) is created to solve the tracking problem. Both MV and IMVC were useful only for minimum-phase systems. Hastings-James and later Clarke [34], modified these control laws by adding a control costing term. Finally, the Generalized Minimum Variance Controller (GMVC) is presented as a complete control algorithm that can control both minimum-phase and non-minimum-phase systems. GMVC was initially formulated for single-input single-output (SISO) systems [35]. Koivo extended this version to the multi-input multi-output (MIMO) case [36]. Through this control approach, a trade-off can be found between minimizing the output error variance and smoothing control variations by selecting suitable weight functions. It is clear that continuous-time controller laws will show a good performance only for a very small sampling-period since it does not take into account the sampling-time in the design procedure. The discrete GMVC considers the sampling period in the design phase and therefore can give better performance, even if the sampling period is considerably large. It is also more suitable for spacecraft onboard computing in practical aspects [37]. Also, the controller designed in the discrete domain also has an advantage in terms of implementation.

Due to the uncertainties and changes in the satellite's dynamic parameters during its lifetime, the adaptive-based controller will definitely perform a better performance than time-invariant ones. In summary, minimum variance control is one of the useful approaches that partially covers the whole set of stated benefits. However, no discussion is made about the use of MVC/GMVC in the field of satellite attitude control so far, despite being of great theoretical and practical interest. So in this paper, we proposed adaptive GMVC as an optimal approach to meet the attitude control requirements of a Hi-Res remote sensing satellite in its imaging phase. This approach uses the RLS algorithm to update the controller parameters in accordance with the changes in dynamics parameters.

# ADCS Operational Modes

To fulfill the control requirements, the ADCS of remote sensing satellites usually contains five basic modes. This section introduces definitions of these modes.

Standby Mode (SM): Just after the orbit injection phase, when the onboard computer is turned on, the ADCS automatically enters standby mode, in which no actions for attitude control are taken. This mode allows ground commands and sends onboard telemetry (satellite's health status). however, sensors and actuators are switched off. in this mode only communication and data transfer with satellite is permitted. Ground control unit command is necessary for the satellite to exit this mode.

Mode of de-tumbling and donstruction of the orbital coordinate system (MDC): De-tumbling mode is the first operational mode of ADCS that actives in orbit. After the satellite is separated from the launcher, it will tumble in an uncontrolled attitude motion. The aim of the detumbling mode is to decrease the angular rate of the satellite from an initial expected value of about 10 °/s to an acceptable value (about 1 °/s) in less than 3 orbital periods. only 3-axis magnetometer and magnitorquers are active in this mode. The popular B-dot algorithm [37] will be used as a control law in MDC mode.

Initial Attitude Acquisition Mode (IAAM): this is an intermediate mode from detumbling to sun pointing mode. At the end of this mode, the spacecraft shall be pointed in nadir (with a pointing accuracy of 15 degrees). A combination of magnetometer, gyro, and magnetorquers is enough to meet the requirements of the IAAM. It should be noted that this mode takes about 30 minutes and the necessary condition to get out of this mode is to observe the sun.

Sun-Pointing Mode (SPM): this mode aims to point the solar panels towards the Sun vector within a tolerance of about $10^{\circ}$ ($3\sigma$), to maximize the electrical power generation and charge the onboard batteries. The SPM uses classical PID to perform its task.

Earth-Pointing Mode (EPM): The EPM aims to point the satellite's camera toward the Earth and to keep the angular rate closed to the specified value (near zero). Due to limitations on the energy available for the ADCS,

the reaction wheels cannot be operated the whole orbit. Thus, it is necessary to switch.

between the 2 different conditions (i) high-precession, and (ii) low-precession in EPM. In high-precession (also called imaging mode) ADCS has to provide pointing accuracy of about $0.1°$ and precession of about 0.015 %s using a combination of reaction wheels' array, magnetometer, fine sun sensors and gyroscope. High precession EPM is the most sensitive mode in the satellite's lifetime because it is directly related to the requirements of the payload. Thus, External disturbances and noise effects cannot be neglected in this mode. In this case, the minimum variance controller is needed to perform the highest precession. High precession EPM lasts only 6 minutes per day (only in the imaging phase).

In the low-precession case, it is enough to point the camera toward the earth with about 3 to 5 degrees as accuracy and about 0.3 %s as precession. So in this condition, a combination of magnetorquers, magnetometer, Sunsensor (only in sun-light), and gyroscope are sufficient. PID controller is effective and suitable for this condition, due to its implementation simplicity and computational effort reduction. It should be noted that reaction wheels' momentum dumping is also performed in this mode.

Emergency Mode (EM): Emergency mode is only activated if there is a malfunction or failure in the ADCS, or when the other modes are unable to operate/run perfectly. In this mode, only magnitorquers and magnetometer are active to keep the satellite rate at about 1 %s. Almost all the other hardware are switching off to minimize energy consumption. Thus, the angular velocity of the satellite is estimated from the magnetometer data. A PD controller is a suitable and effective algorithm for this condition.

Note: Attitude Determination and Estimation Mode (ADEM): In fact, the ADEM is not a real operating mode, since the computations for attitude determination and estimation are almost done in all modes, except the SM and DE-tumbling mode. It is considered a true mode due to the necessity of attitude knowledge even when the attitude is not being stabilized or controlled.

In this paper, we concentrated only on the high-precession EPM. Fig.3 shows the active and passive hardware in different operational modes. In this picture, the gray color is used for active cases, and the white color is used for inactive ones.

The sequence flow and relation of different control modes over the satellite's lifetime are shown in Fig. 4.

The blue and black lines represent the paths that are taken autonomously and with the help of the ground station command (GSC), respectively.
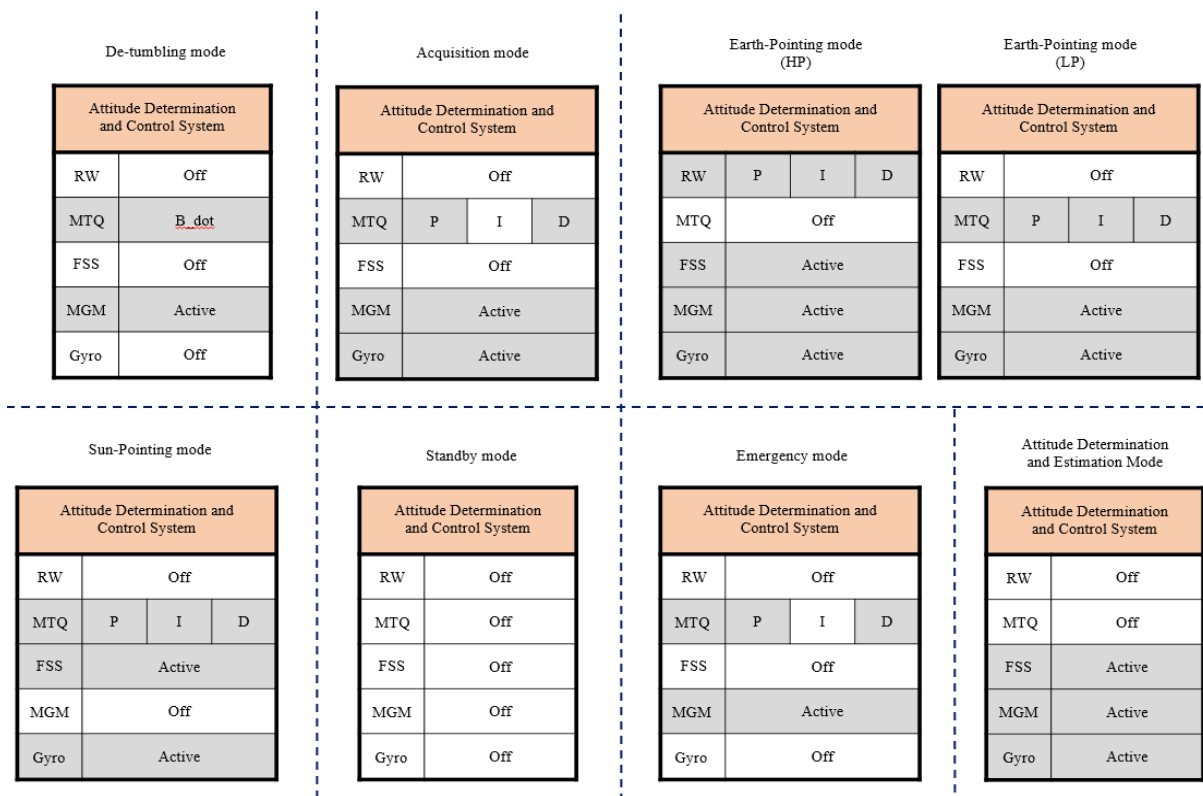
**De-tumbling mode**

| Attitude Determination and Control System | |
|---|---|
| RW | Off |
| MTQ | B_dot |
| FSS | Off |
| MGM | Active |
| Gyro | Off |

**Acquisition mode**

| Attitude Determination and Control System | | | |
|---|---|---|---|
| RW | Off | | |
| MTQ | P | I | D |
| FSS | Off | | |
| MGM | Active | | |
| Gyro | Active | | |

**Earth-Pointing mode (HP)**

| Attitude Determination and Control System | | | |
|---|---|---|---|
| RW | P | I | D |
| MTQ | Off | | |
| FSS | Active | | |
| MGM | Active | | |
| Gyro | Active | | |

**Earth-Pointing mode (LP)**

| Attitude Determination and Control System | | | |
|---|---|---|---|
| RW | Off | | |
| MTQ | P | I | D |
| FSS | Off | | |
| MGM | Active | | |
| Gyro | Active | | |

**Sun-Pointing mode**

| Attitude Determination and Control System | | | |
|---|---|---|---|
| RW | Off | | |
| MTQ | P | I | D |
| FSS | Active | | |
| MGM | Off | | |
| Gyro | Active | | |

**Standby mode**

| Attitude Determination and Control System | |
|---|---|
| RW | Off |
| MTQ | Off |
| FSS | Off |
| MGM | Off |
| Gyro | Off |

**Emergency mode**

| Attitude Determination and Control System | | | |
|---|---|---|---|
| RW | Off | | |
| MTQ | P | I | D |
| FSS | Off | | |
| MGM | Active | | |
| Gyro | Off | | |

**Attitude Determination and Estimation Mode**

| Attitude Determination and Control System | |
|---|---|
| RW | Off |
| MTQ | Off |
| FSS | Active |
| MGM | Active |
| Gyro | Active |

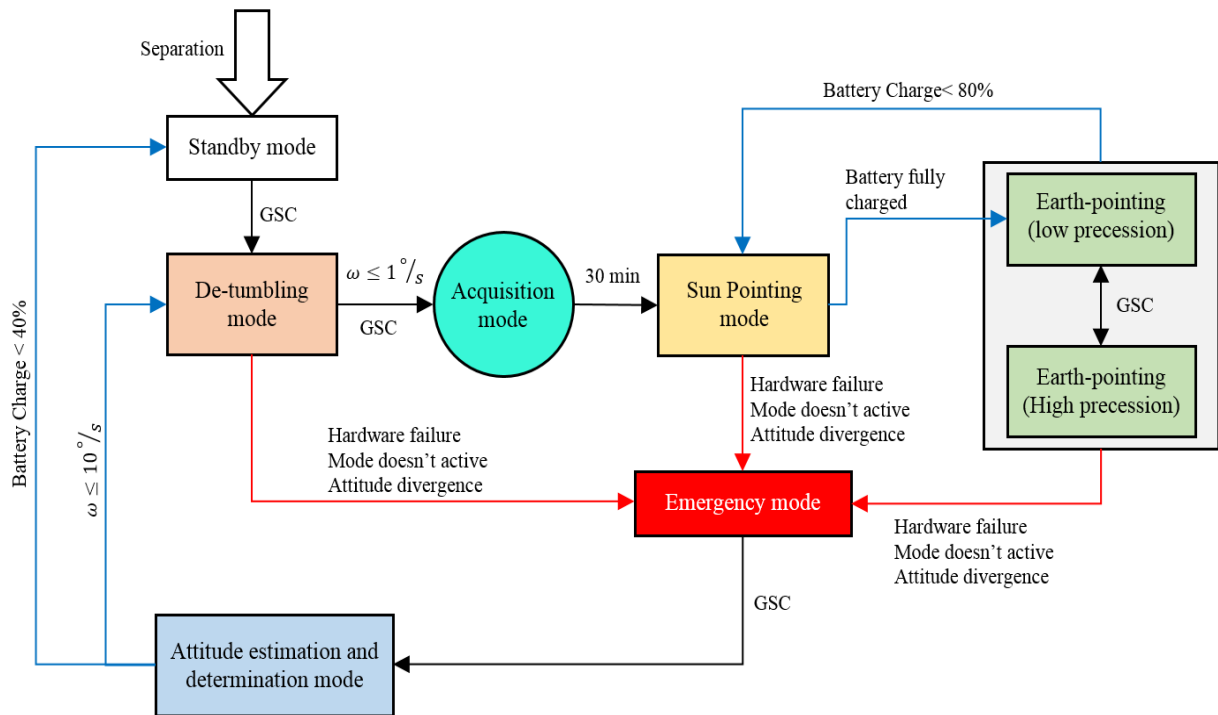**Fig. 3.** Attitude control system modes of operation

**Fig. 4.** Relation of ADCS operational modes

# Mathematical Modeling

Definition of Some coordinate systems is necessary for driving and analyzing the rotational motion of the spacecraft, which are defined in this section.

## Coordinate Systems

- Earth-Centered Inertial (ECI) coordinate system $(O_I, X_I, Y_I, Z_I)$

$O_I$- the origin of the coordinate system is located at the center of the earth
$X_I$- Directed to the vernal equinox
$Y_I$- Completes right-hand rule
$Z_I$- Coincident with the Earth's axis of rotation in the direction of the north pole.

- Orbit Reference coordinate system $(O_r, X_r, Y_r, Z_r)$

$O_r$- is located at the center of mass (cm) of the satellite and moves with it
$X_r$ - in the orbital plane, in the direction of the satellite's velocity vector
$Y_r$- normal to the orbital plane & complete a 3-axis right-hand orthogonal system
$Z_r$- points toward the cm of the Earth

- Body coordinate system $(o_b, x_b, y_b, z_b)$.

$o_b$- is located at the cm of the satellite and moves with it
$x_b, y_b, z_b$ - axes of the body coordinate system are aligned with the axes of the orbit reference coordinate system and are fixed to the principal moments of inertia of the spacecraft

Fig. 5 shows a schematic geometry of the mentioned coordinate systems. The deviation of the body coordinate system from the orbital coordinate system is called attitude motion. The camera is located in the direction of $+z_b$. Nadir pointing refers to the conditions in which the body and orbital coordinate systems coincide
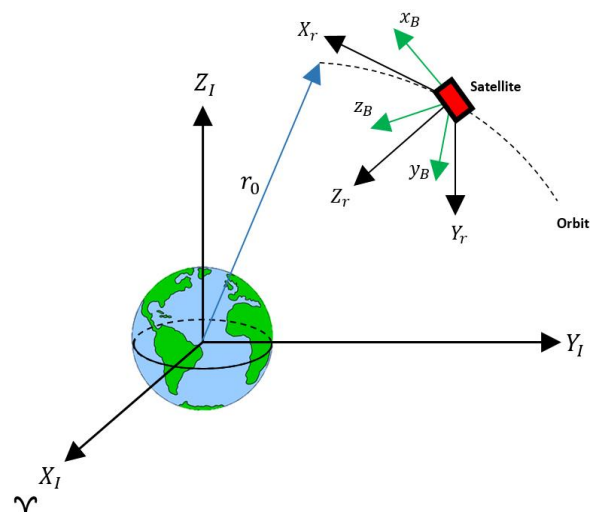


**Fig. 5.** Definition of coordinate systems

In the case of remote sensing satellites, the nadir attitude is of particular importance because the satellite must be in nadir condition during the imaging phase

# Continuous-Time Dynamic Model

The dynamics equation actually represents the relation between the torques applied to spacecraft and the body angular rate. The dynamic model of a satellite is given by the Euler's rotational equation as:

$$\dot{H}_I = \dot{H}_B + \left(\omega^{B/I} \times H_B\right)$$

$$\dot{H}_I = T_{Ext} \tag{1}$$

where $T_{Ext} = \left[T_x, T_y, T_z\right]^T \epsilon \Re^3$ is the external torque acting on the satellite and $H_I = \left[H_x, H_y, H_z\right]^T \epsilon \Re^3$ is body angular momentum in the inertial coordinate system. $\omega^{B/I} = \left[\omega_x, \omega_y, \omega_z\right]^T \epsilon \Re^3$ denotes the angular velocity vector of the body frame with respect to the Inertial reference frame. $H_B = \left[h_x, h_y, h_z\right]^T \epsilon \Re^3$ is the angular momentum vector of a rigid satellite about its center of mass. Unlike thrusters that apply external torque to the satellite and change the momentum of the entire system, the wheels are internal components of the satellite and only change the angular momentum distribution of the system. Thus, the entire system's angular momentum is:

$$H_B = h_{sat} + h_w \tag{2}$$

where $h_{sat} = I\omega^T \epsilon \Re^3$ and $h_w = \left[h_{w_x}, h_{w_y}, h_{w_z}\right]^T \epsilon \Re^3$ are the satellite's body and reaction wheels' angular momentum, respectively. $I = \begin{bmatrix} I_x & I_{xy} & I_{xz} \\ I_{yx} & I_y & I_{yz} \\ I_{zx} & I_{zy} & I_z \end{bmatrix} \epsilon \Re^{3\times3}$

is the satellite inertia tensor

Using Eqs. (1) and (2), it can be written:

$$T_{Ext} = I\dot{\omega} - u + \omega^{B/I} \times (I\omega + h_w) \tag{3}$$

where $u = -\dot{h}_w \epsilon \Re^3$ is the control torque of the reaction wheel.

Finally, the nonlinear dynamics of a spacecraft equipped with RWs are given in equation (4) [30].

$$\sum T_x = \left[\dot{h}_x + \dot{h}_{w_x} + \left(\omega_y h_z - \omega_z h_y\right) \right.$$
$$\left. + \left(\omega_y h_{wz} - \omega_z h_{wy}\right)\right]$$
$$\sum T_y = \left[\dot{h}_y + \dot{h}_{w_y} + \left(\omega_z h_x - \omega_x h_z\right) \right.$$
$$\left. + \left(\omega_z h_{wx} - \omega_x h_{wz}\right)\right] \tag{4}$$
$$\sum T_z = \left[\dot{h}_z + \dot{h}_{w_z} + \left(\omega_x h_y - \omega_y h_x\right) \right.$$
$$\left. + \left(\omega_x h_{wy} - \omega_y h_{wx}\right)\right]$$

## Continuous Time Kinematic Model

The kinematic equation in fact represents the relation of body angular rate (measured by the 3-axis gyroscope) and Euler angles change rate. The kinematic model of a rigid body based on Euler angle parameterization is given in Eq. (5) [30].

$$\begin{bmatrix} \dot{\phi} \\ \dot{\theta} \\ \dot{\psi} \end{bmatrix} =$$
$$\frac{1}{\cos\theta}\begin{bmatrix} \cos\theta & \sin\phi\sin\theta & \cos\phi\sin\theta \\ 0 & \cos\phi\cos\theta & -\sin\phi\cos\theta \\ 0 & \sin\phi & \cos\phi \end{bmatrix}\begin{bmatrix} \omega_x \\ \omega_y \\ \omega_z \end{bmatrix} \tag{5}$$

where, $\psi, \theta$, and $\phi$ are the Euler angles.

## Gravity Gradient Torque Modeling

The spacecraft body is subject to a non-uniform gravity field which can cause external torques about the body center. This non-uniformity is due to the nonhomogeneous distribution of spacecraft mass along the main axes [30]. Therefore, gravity gradient torque which is the dominant disturbance in LEO can be modeled as Eq. (6).

$$T_{GG_x} = \frac{3\mu}{2r_0^3}\left(I_z - I_y\right)sin(2\phi)cos^2(\theta)$$
$$T_{GG_y} = \frac{3\mu}{2r_0^3}\left(I_z - I_x\right)sin(2\theta)cos(\phi) \tag{6}$$
$$T_{GG_z} = \frac{3\mu}{2r_0^3}\left(I_x - I_y\right)sin(2\theta)sin(\emptyset)$$

$\mu = 3.986 \times 10^{14}\frac{m^3}{s^2}$ is the Earth's gravitational parameter $r_0$ represents the distance from the center of the Earth to the center of gravity of the satellite. In this paper, we assumed the earth as a full sphere with a radius of 6378 km.

## Linearization

Remote sensing satellites spend most of their orbital life in Nadir-pointing attitude. Thus in this section, the equations of motion will be linearized around the stable nadir condition $([\psi, \theta, \phi] = [0, 0, 0])$ and then discretized in the next chapter.

By integrating the dynamics and kinematic equations, the linearized equations of motion in the presence of gravity-gradient disturbance torque will be as follows [39].

$$T_{cx} = I_x\ddot{\phi} + 4\omega_0^2(I_y - I_z)\phi + \omega_0(I_y - I_z - I_x)\dot{\psi} + \dot{h}_{wx} - \omega_0 h_{wz} - I_{xy}\ddot{\theta} - I_{xz}\ddot{\psi} - I_{xz}\omega_0^2\psi + 2I_{yz}\omega_0\dot{\theta}$$

$$T_{cy} = I_y\ddot{\theta} + 3\omega_0^2(I_x - I_z)\theta + \dot{h}_{wy} - I_{xy}(\ddot{\phi} - 2\omega_0\dot{\psi} - \omega_0^2\phi) + I_{yz}(-\ddot{\psi} - 2\omega_0\dot{\phi} - \omega_0^2\psi) \tag{7}$$

$$T_{cz} = I_z\ddot{\psi} + \omega_0^2(I_y - I_x)\psi + \omega_0(I_z + I_x - I_y)\dot{\phi} + \dot{h}_{wz} + \omega_0 h_{wx} - I_{yz}\ddot{\theta} - I_{xz}\ddot{\phi} - I_{xz}\omega_0^2\phi - 2I_{xy}\omega_0\dot{\theta}$$

Assuming the non-diagonal elements of inertia tensor $([I_{xy}, I_{xz}, I_{yz}])$ are zero, the state space format of the equation (7) will be as follows:

$$\dot{X} = [A]X + [B]T_C \qquad (8)$$

$X = [\phi, \theta, \psi, \dot{\phi}, \dot{\theta}, \dot{\psi}]^T$ denotes the state vector, and $T_C = [T_{c_x}, T_{c_y}, T_{c_z}]^T$ denotes the control input vector.

In Eq. (8), Matrices $[A]$ and $[B]$ are defined as follows:

$$[A] = \begin{bmatrix} 0 & 0 & 0 & 1 & 0 & 0 \\ 0 & 0 & 0 & 0 & 1 & 0 \\ 0 & 0 & 0 & 0 & 0 & 1 \\ a_{41} & 0 & 0 & 0 & 0 & a_{46} \\ 0 & a_{52} & 0 & 0 & 0 & 0 \\ 0 & 0 & a_{63} & a_{64} & 0 & 0 \end{bmatrix},$$

$$[B] = \begin{bmatrix} 0 & 0 & 0 \\ 0 & 0 & 0 \\ 0 & 0 & 0 \\ b_{41} & 0 & 0 \\ 0 & b_{52} & 0 \\ 0 & 0 & b_{63} \end{bmatrix}$$

where $a_{41} = \frac{4\omega_0^2(I_z - I_y)}{I_x}$, $a_{46} = \frac{\omega_0(I_x + I_z - I_y)}{I_x}$, $a_{52} = \frac{3\omega_0^2(I_z - I_y)}{I_y}$, $a_{63} = \frac{\omega_0^2(I_x - I_y)}{I_z}$, $a_{64} = \frac{(I_y - I_z - I_x)\omega_0}{I_z}$, $b_{41} = \frac{1}{I_x}$, $b_{52} = \frac{1}{I_y}$, $b_{63} = \frac{1}{I_z}$, and $\omega_0$ represents the orbital frequency (orbital mean motion) that is equal to $\sqrt{\mu/r_0^3}$.

### Discretization

The controller law should be processed in a digital computer with a specific frequency. Therefore, Significant benefits from an implementation perspective are realized for digital controllers [40]. a simple block diagram of a computer-based control system is depicted in Fig. 6 [41]. the point is we need to discretize the equation of motion to be able to design the GMVC.
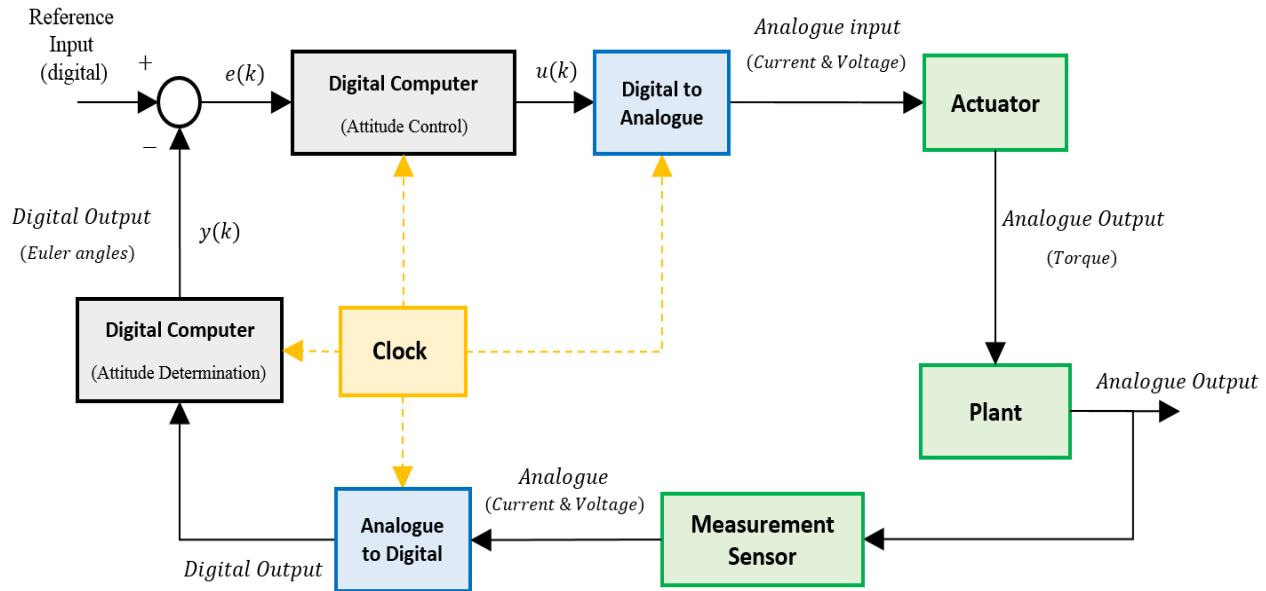


**Fig. 6.** block diagram of a computer-based (digital) control system

Equation (9) shows the standard form of a discrete-time transfer function:

$$\frac{y(k)}{u(k)} = \frac{B(q^{-1})}{A(q^{-1})}$$
$$= \frac{q^{-d}(b_0 + b_1 q^{-1} + \cdots + b_m q^{-m})}{1 + a_1 q^{-1} + a_2 q^{-2} + \cdots + a_n q^{-n}} \qquad (9)$$
$$d > 0 \; ; \; b_0 \neq 0 \; ; y(0) \neq 0$$

which $q^{-1}$ is the backward shift operator. Also $d$, $y(k)$ and $u(k)$ are delay, output, and input of the system, respectively. $A(q^{-1})$ and $B(q^{-1})$ are the polynomials of the numerator and denominator of the discrete-time transfer function which are unknown in this paper. These two polynomials are defined as follows:

$$B(z^{-1}) = b_0 + b_1 z^{-1} + \cdots + b_{N_B} z^{N_B}$$
and $b_0 \neq 0$ \qquad (10)

$$A(z^{-1}) = 1 + a_1 z^{-1} + a_2 z^{-2} + \cdots + a_{N_A} z^{-N_A}$$

Exact discretization may sometimes be intractable due to the heavy matrix exponential and integral operations involved. Thus it is much easier to calculate an approximate discrete model. In this case, Euler's numerical method can be used to transform Eq. (7) into its equivalent discrete-time equation, as follows:

$$\dot{x} = f(x(t), u(t))$$
$$\frac{x(t+1) - x(t)}{\Delta t} = f(x(t), u(t)) , \Delta t = T_s \qquad (11)$$

where $T_s$ represents the sampling period, which should be small enough.

Therefore, the discrete-time form of equation. (7) can be written as equation. (12).

$$
\begin{aligned}
T_{Cx} &= I_{xx}\frac{\phi(t+2)-2\phi(t+1)+\phi(t)}{T_s^2} \\
&+ 4\omega_0^2(I_{yy}-I_{zz})\phi(t) \\
&+ \omega_0(I_{yy}-I_{zz}-I_{xx})\left(\frac{\psi(t+1)-\psi(t)}{T_s}\right) \\
&- I_{xy}\frac{\theta(t+2)-2\theta(t+1)+\theta(t)}{T_s^2} \\
&- I_{xz}\frac{\psi(t+2)-2\psi(t+1)+\psi(t)}{T_s^2} \\
&- I_{xz}\omega_0^2\psi(t)+2I_{yz}\omega_0\frac{\theta(t+1)-\theta(t)}{T_s} \\[6pt]
T_{Cy} &= I_{yy}\frac{\theta(t+2)-2\theta(t+1)+\theta(t)}{T_s^2} \\
&+ 3\omega_0^2(I_{xx}-I_{zz})\theta(t) \\
&+ I_{xy}\left(\frac{\phi(t+2)-2\phi(t+1)+\phi(t)}{T_s^2}\right. \\
&\left. -2\omega_0\frac{\psi(t+1)-\psi(t)}{T_s}-\omega_0^2\phi(t)\right) \\
&+ I_{yz}\left(-\frac{\psi(t+2)-2\psi(t+1)+\psi(t)}{T_s^2}\right. \\
&\left. -2\omega_0\frac{\phi(t+1)-\phi(t)}{T_s}+\omega_0^2\psi(t)\right) \\[6pt]
T_{Cz} &= I_{zz}\frac{\psi(t+2)-2\psi(t+1)+\psi(t)}{T_s^2} \\
&+ \omega_0^2(I_{yy}-I_{xx})\psi(t) \\
&+ \omega_0(I_{xx}+I_{zz}-I_{yy})\left(\frac{\phi(t+1)-\phi(t)}{T_s}\right) \\
&- I_{yz}\frac{\theta(t+2)-2\theta(t+1)+\theta(t)}{T_s^2} \\
&- I_{xz}\frac{\phi(t+2)-2\phi(t+1)+\phi(t)}{T_s^2} \\
&- I_{xz}\omega_0^2\phi(t)+2I_{xy}\omega_0\frac{\theta(t+1)-\theta(t)}{T_s}
\end{aligned}
\tag{12}
$$

The continuous-time state-space model in Equation (9) can be discretized to get the discrete-time state-space model as follows:

$$X(k+1) = GX(k) + Hu(k-d) \tag{13}$$

where $G\epsilon R^{n\times n}$ and $H\epsilon R^{n\times 1}$ are the discrete-time state-space matrices which can be computed as Eq. (14). $X(k)$ denotes the state vector. $d$ represent the number of delay samples and as clear as Eq. (12) is equal to 2 (system's pure delay).

$$
\begin{aligned}
G &= e^{AT} \\
H &= \left[\int_0^T e^{AT}\,dt\right]B
\end{aligned}
\tag{14}
$$

**ADCS's Active Hardware in Imaging Phase**

**Attitude Determination Sensor**

To maintain the stability of a spacecraft and control its attitude, two principal types of attitude determination hardware should be used: (i) attitude sensor for Euler angles measurement and (ii) Inertia Measurement Unit (IMU) for body angular velocity measurement. In general, the selection of a particular attitude sensor will depend on the required pointing accuracy, precession, and also the tasks or mission to be fulfilled by the spacecraft.

We assumed that the satellite was equipped with a 3-axis magnetometer, three 2-axis sun-sensor "SS-411" and, two 3-axis rate-gyro "STIM210". It's well known that at least 2 sources (or 2 references) are needed for full attitude determination (without singularity). For example, a combination of earth sensor and sunsensor, or a combination of magnetometer or sunsensor. In this paper, we assumed that sunsensors and magnetometer are covering each other. Magnetometers are very important, reliable, and useful sensors in low earth orbit that don't depend on sunlight. Especially, They are essential for detumbling phase. But unlike sunsensors, magnetometers provide analogue output and its noise and other specifications are different from sunsensors or rate gyros. So in this work we doesn't take into account the noise of magnetometers output.

The statistical noise level of "SS-411" is low, of the order of 0.1 degrees (RMS), depending also on the dynamic range of the instrument's output and ambient temperature. The SS-411 sun-sensor is shown in Fig. 7.



**Fig. 7.** SS-411 Sun-sensor

The SS-411 sun sensor specifications are presented in the following Table.

**Table.2.** SS-411 Sun-sensor specifications [42]

| Accuracy | Field of view | Mass | Temperature |
|---|---|---|---|
| $\pm 0/1$ deg | $\pm 70$ deg | 34 gr | $-25\ to+70℃$ |
| **Update Rate** | **Supply Voltage** | **Supply Current** | **RMS** |
| 5 Hz | 5-50 V | 7/5 to 27 mA | 0/1 deg |

STIM210 is a cluster of 3 orthogonal high-accuracy(fine) MEMS-based gyros in a miniature package. The use of this instrument is not dependent on

the spacecraft's orientation in space. This is an advantage over the earth, star, and sun sensors, whose signal source must be within their optical fields of view (FOV). STIM210 rate-gyro presents low noise and low bias instability. It also performs excellent performance in vibration and shock environments which makes it useful for remote-sensing missions. The STIM210 rate-gyro is shown in Fig.8.
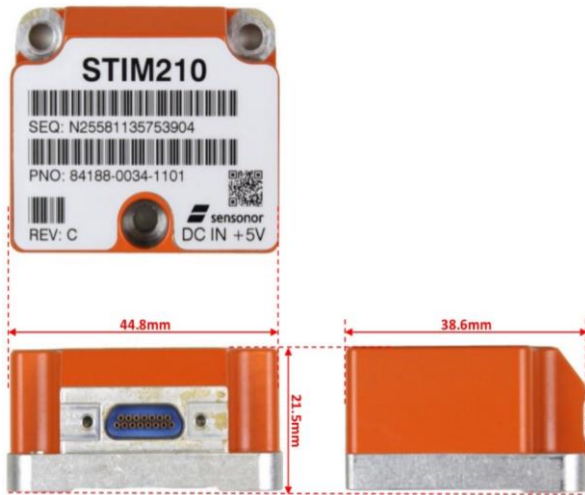


**Fig. 8.** STIM210 Rate-gyro

The STIM210 rate-gyro specifications are presented in Table 3.

**Table. 3.** STIM210 Rate-gyro specifications [43]

| Bias instability | Input range | Mass | Temperature |
|---|---|---|---|
| 0/5 deg/h | $\pm$400 deg/s | 52 gr | $-40$ to $+85°C$ |
| **Interface** | **Supply Voltage** | **Supply Current** | **RMS** |
| RS422 | 4/5 to 5/5 V | 150 to 500 mA | 0/15 deg/s |

## Attitude Control Actuator

RWs generate serious disturbances, particularly periodic disturbances called parasitic micro-vibrations. There are two major micro-vibration sources in reaction wheels, (i) Rotor unbalances and (ii) Ball bearing vibration.

Rotor unbalance is the uneven distribution of mass around an axis of rotation. The unbalance of a rotor consists of two types: static unbalance and dynamic unbalance (see more details in bong wie [44]).

The static unbalance causes vibration forces in the plane of rotation. The dynamic unbalance causes a "wobbly rotor", i.e., vibration moments out of the plane

of rotation. The RWs' unbalance is known as a major disturbing factor to cause imaging distortion/deformation in imaging mode [45].

Ball-bearing vibration is mainly due to the weakness of construction and technology. Bearing rings and balls are not perfectly round, it means that the balls and raceways, even after extensive fine grinding and polishing, are not still perfectly smooth. Excessive vibration will increase bearing noise and can drastically shorten the life of a bearing. Fig.9 shows a typical RW part.
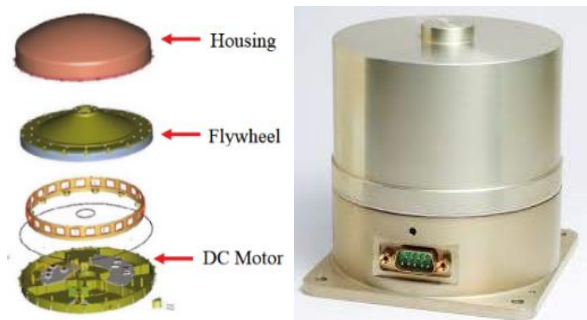


**Fig. 9.** NRWA-T10 Reaction wheel

The NRWA-T10 reaction wheel is capable to produce high torque (more than 0.2 Nm) and angular momentum storage capacity (more than 10 Nms), which makes it ideal for agile medium to large micro-satellites requiring both maneuverability and accurate pointing. So, we chose NRWA-T10 as the ACS actuators.

The NRWA-T10 RW specifications are presented in Table 4.

**Table. 4.** NRWA-T10 Reaction wheel specifications [46]

| Max Torque | Max RPM | Mass | Temperature |
|---|---|---|---|
| 0/21 Nm | $\pm$6000 RPM | 5 kg | $-5$ to $+60°C$ |
| **Inertia** | **Speed control accuracy** | **Power** | **RMS** |
| 0/02 kg. m$^2$ | 0/6 RPM | 18 W | 0/2 Nm |

## Noise Modeling

Fig.10 shows a control configuration concept using the sun-sensor, rate gyro, and reaction wheel together. The parasitic noises pertaining to the sensors are indicated as $WN_{RS}$ for the rate sensor noise, $WN_{PS}$ for the attitude position sensor noise and $WN_{RW}$ for reaction wheel torque noise [30].
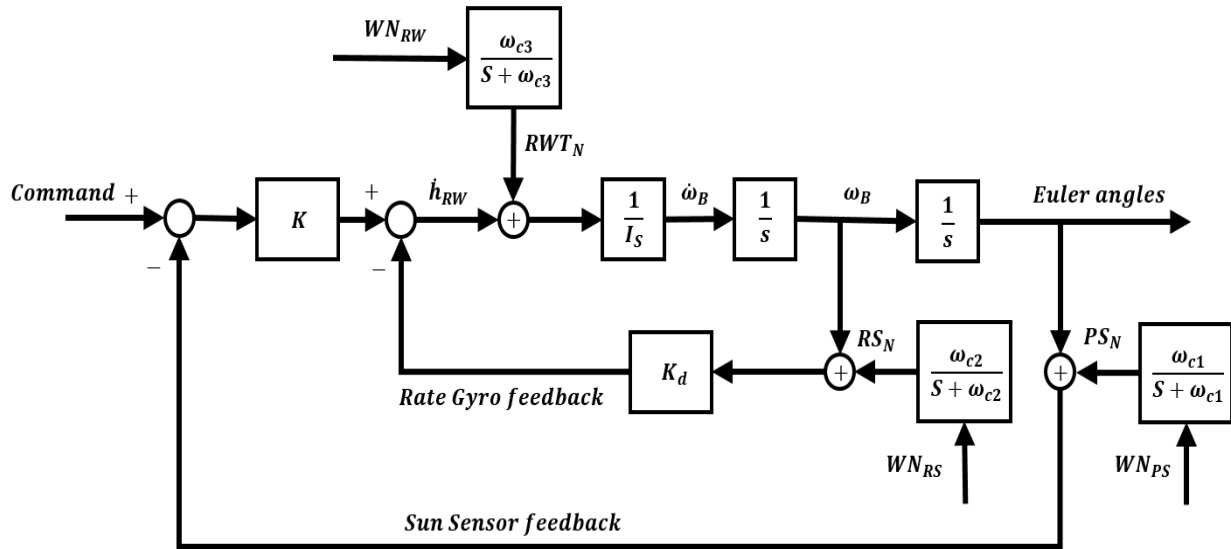
**Fig. 10.** Reaction wheeled ACS concept [30]

In the following analysis, it is theoretically possible to deal with the ideal white noise, whose power spectral density (PSD) function is uniform with amplitude WN. However, white noise does not exist in real-world conditions; so, the noise existing in engineering problems is colored too. We will model a colored noise (as a sensor and actuator parasitic noise), by passing the Gaussian White Noise (GWN) through a first-order filter with the corner frequency of $\omega_c$. The relation between the amplitude of the GWN and the mean square (MS) value of the colored noise is defined as follows [30].

$$x^2 = 0.5WN_{hardware}\omega_c \tag{15}$$

where $x$ is the Root-Mean-Square (RMS) value of the colored noise.

Table 5 shows the noise specification of each component.

**Table.5.** Noise specification of components

| Parameter | Value |
|-----------|-------|
| $\omega_{c1} = \omega_{c2} = \omega_{c3}$ | $100\ rad/s$ |
| $WN_{PS}$ | $6/0923 \times 10^{-8}$ |
| $WN_{RS}$ | $1/3708e - 07$ |
| $WN_{RW}$ | $8 \times 10^{-4}$ |

RMS of PS, RW and RS noise are plotted in Fig. 11.
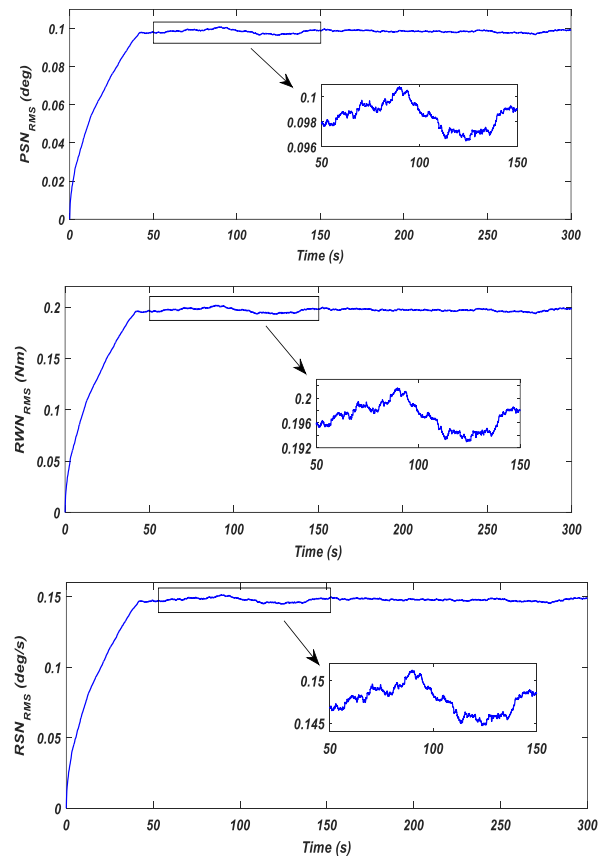


**(contionation) Fig. 11.** RMS of hardware noise

## Controller Design

This chapter first introduces the MV Regulator and then will develop the IMV and GMV controller.

## Minimum Variance Regulator

The standard equation of a linear system in the presence of noise is written as follows (ASTROM (1970) model).

$$y(t) = \frac{B(q^{-1})}{A(q^{-1})} u(t) + \frac{C(q^{-1})}{A(q^{-1})} e(t) \qquad (16)$$

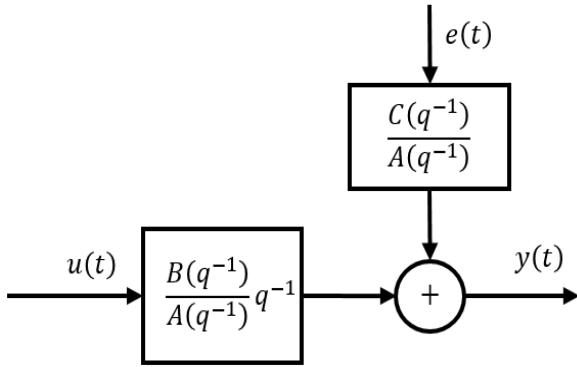Fig. 12 shows the block diagram of the above equation.



**Fig. 12.** Flow chart of the ASTROM model

which, $B(q^{-1})$ and $A(q^{-1})$ are of order $m$ and $n$, respectively. $C(q^{-1})$ is a stable monic polynomial of order $n$ that presents noise dynamics.

$$C(q^{-1}) = 1 + c_1 q^{-1} + c_2 q^{-2} + \cdots + c_n q^{-n} \qquad (17)$$

In steady-state regulation, it makes sense to express the criteria in terms of the steady-state variances of the output and the control signals. This leads to The MV regulator cost function (performance criterion).

$$J = E\{y^2(t) + \rho u^2(t)\} \qquad (18)$$

which $E$ is the mathematical expected value (with respect to the noise process acting on the system). generally, the control law which minimizes Eq. (18) is the "linear quadratic Gaussian (LQG)". In a specific condition where $\rho$ is equal to zero, the resulting controller is called the "minimum-variance controller". In other words, the MV controller/regulator provides the regulation goal with any amount of control effort. Therefore, minimum-variance control can be considered as a subset of the optimal control theory.

The forecast horizon of the MV approach is equal to the system's pure delay $(d)$. The predictive output is shown in Eq. (19).

$$y(t + d) = \frac{B}{A} u(t + d) + Fe(t + 1) \\ + \frac{qG}{A} e(t) \qquad (19)$$

Following Equation 19, the system output is predicted in d sample times later and then the proper control signal will be determined to ensure that the output variance is as close as the white noise variance.

$F$ and $G$ are the polynomials that are calculated by following the Diophantine equation.

$$q^{d-1} C = A(q^{-1}) F(q^{-1}) + G(q^{-1}) \qquad (20)$$

F is a monic polynomial of order $(d - 1)$, and G is of $(n - 1)$th order, as shown in Eq. 21.

$$F(q) = q^{d-1} + f_1 q^{d-2} + \cdots + f_{d-1}$$
$$G(q) = g_0 q^{n-1} + g_1 q^{n-2} + \cdots + g_{n-1} \qquad (21)$$

Using Eq. (16), we can propose the following relation as an observer for noise.

$$e(t) = \frac{A}{C} y(t) - \frac{B}{C} u(t) \qquad (22)$$

By a combination of equations (19) and (21), equation 23 is obtained.

$$y(t + d) = Fe(t + d) + \frac{qBF}{C} u(t) + \frac{qG}{C} y(t) \qquad (23)$$

In Eq. (14), the term $Fe(t + d)$ is not predictable due to its stochastic nature, therefore it cannot be controlled. The control goal would be achieved if the term $\frac{qBF}{C} u(t) + \frac{qG}{C} y(t)$ were removed from relation (23). So, the control signal can be written as follows.

$$u(t) = -\frac{G}{BF} y(t) \qquad (24)$$

On that account, predicted output and prediction error can be stated as Eq. (25) and (26), respectively.

$$\hat{y}(t + d|t) = \frac{qBF}{C} u(t) + \frac{qG}{C} y(t) \qquad (25)$$

$$\tilde{y}(t + d|t) = y(t + d) - \hat{y}(t + d|t) \\ = Fe(t + d) \qquad (26)$$

According to the available information up to the moment (t), the output variance at the moment $(t + d)$ is described as Eq. (27).

$$var\tilde{y}(t + d_0|t) = \sigma^2 (1 + f_1^2 + f_2^2 + \cdots + f_{d_0 - 1}^2) \qquad (27)$$

Finally, the system's output at the moment $(t + d_0)$ will be as follows.

$$y(t + d_0)_{min} = Fe(t + 1) \qquad (28)$$

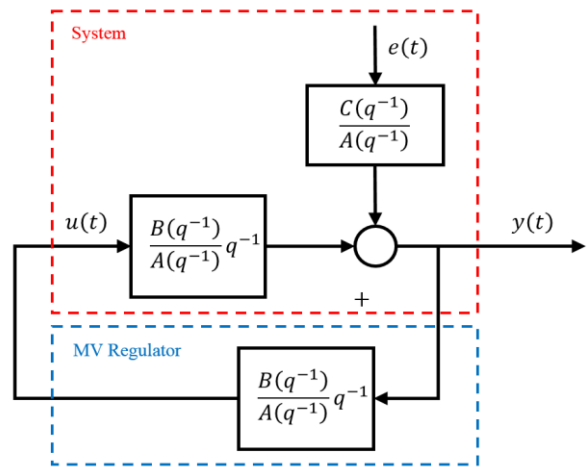Fig. 13 shows the block diagram of the MV regulator.



**Fig. 13.** Flow chart of the MV regulator

Assuming the satellite's weight and shape to be symmetrical ($I_{xx} = I_{yy} = I_{zz}$), According to Eqs. (12) and (13), the system transfer function can be written as follows.

$$H(q^{-1}) = q^{-2} \frac{b_0}{q^{-2} + a_1 q^{-1} + a_2} \tag{29}$$

where $a_1 = -2$, $a_2 = 1$ and $b_0 = \frac{T_s^2}{I_{xx}}$ are exact values of dynamic parameters which will be estimated from the RLS identification system. In Eq. (29), the system pure delay ($d_0$) is 2 sample times.

To solve the Diophantine equation, the C polynomial must be selected first. This polynomial represents the error dynamics and should be stable. The C polynomial degree is as same as A, which we selected as follows.

$$\begin{aligned} C(q^{-1}) &= (z - 0.001)(z - 0.002) \\ C(q^{-1}) &= q^2 + c_1 q^1 + c_2 \end{aligned} \tag{30}$$

where $c_1 = -0.003$ and $c_2 = 2 \times 10^{-6}$.
$F$ and $G$ are from order 1 and proposed as follows.

$$\begin{aligned} F(q^{-1}) &= 1 + f_1 q^{-1} \\ G(q^{-1}) &= g_0 + g_1 q^{-1} \end{aligned} \tag{31}$$

Now it is possible to calculate F and G from the Diophantine equation mentioned in Eq. (20).

$$q(q^2 + c_1 q^1 + c_2) = (q^2 + a_1 q^1 + a_2)(q + f_1) + (g_0 q + g_1) \tag{32}$$

As a result, the output of the Diophantine equation is $f_1 = c_1 - a_1$, $g_1 = -a_2 f_1$, $g_0 = c_2 - a_2 - a_1 f_1$.
Finally, the control signal is calculated as follows.

$$u(t) = -\frac{g_0}{b_0} y(t) - \frac{g_1}{b_0} y(t-1) - f_1 u(t-1) \tag{33}$$

As the dynamic parameters of the system ($a_1, a_2, b_0$) are identified online, the controller parameters ($f_1, g_0, g_1$) are calculated online as well.

**Extended Least Square Identification Method**
Least squares (LS) is an adaptive filter algorithm that recursively finds the coefficients that minimize a weighted linear least-squares cost function relating to the input signals, which was discovered by " Johann Carl Friedrich Gauss". He formulated the principles of the least square (LS) to determine the orbit of planets. The main disadvantage of this algorithm is that it is offline and cannot be used for real-time applications. Therefore, it was upgraded to the recursive one (RLS). The RLS aims to minimize the following cost function.

$$V(\theta, N) = \frac{1}{2} \sum_{i=1}^{N} (y(i) - \hat{y}(i))^2 \tag{34}$$

where $y(i)$ is the actual output of the system and $\hat{y}(i)$ is the estimated output which is defined as follows.

$$\begin{aligned} \hat{y}(i) &= \varphi_1(t)\theta_1 + \varphi_2(t)\theta_2 + \cdots + \varphi_n(t)\theta_N \\ &= \varphi^T(t)\theta \end{aligned} \tag{35}$$

$\theta$ is the unknown parameters-vector of the mathematical model, and $\varphi^T$ includes the known functions, which are called regression variables. In our case study, according to the transfer function of Eq. (29), the parameters-vector is $\theta = [a_1, a_2, b_0]$ and the regression variable is $\varphi^T(t) = [-y(t-1), -y(t-2), u(t-2)]$.
Now we need to define $\Phi$ and P as follows.

$$\Phi = \begin{bmatrix} \varphi^T(1) \\ \vdots \\ \varphi^T(N) \end{bmatrix} \text{ and } \Phi^T(t)\Phi(t) \neq 0$$

$$P = (\Phi^T(t)\Phi(t))^{-1} = \left( \sum_{i=1}^{t} \varphi(i)\varphi^T(i) \right)^{-1} \tag{36}$$

$P$ is a square diagonal matrix called covariance matrix (CM) .
Finally, the estimated parameters-vector can be written as follows.

$$\hat{\theta}(t) = \hat{\theta}(t-1) + K(t)\left(y(t) - \varphi^T(t)\hat{\theta}(t-1)\right) \tag{37}$$

where, $\varphi^T(t)\hat{\theta}(t-1)$ is known as $\hat{y}(t-1)$ and the term $e(t) = y(t) - \varphi^T(t)\hat{\theta}(t-1)$ is known as the prediction error or the estimation error.

$K(t)$ is known as the correction gain or the Kalman gain which is defined as follows.

$$K(t) = P(t-1)\varphi(t)\left(\lambda I + \varphi^T(t)P(t-1)\varphi(t)\right)^{-1} \tag{38}$$

And P is updated in each step using Eq. (39)

$$P(t) = \frac{(I - K(t)\varphi^T(t))P(t-1)}{\lambda} \tag{39}$$

$I$ is a unit Diagonal matrix, $\lambda$ is known as the forgetting factor. The suitable and conventional value of $\lambda$ is between 0 and 1, little amounts of this parameter increase the sensitivity of the identification algorithm to sudden changes, which may lead to divergence, so we chose it for 0.98.

We need to choose the initial condition P(0) for the covariance matrix. A big initial condition of CM increases the convergence rate. So we choose it as follows.

$$P(0) = \alpha I, \text{ and } \alpha = 10^2 \tag{40}$$

The RLS has been upgraded to the Extended-Least-Squares (ELS) to estimate stochastic phenomena. To derive the ELS identification method without loss of generality, we need to make only a few changes. First, $\varepsilon(t)$ is defined as a noise estimator.

$$\varepsilon(t) = y(t) - \varphi^T(t-1)\hat{\theta}(t-1) \tag{41}$$

The following equation is used for updating parameters instead of Eq. (37).

$$\hat{\theta}(t) = \hat{\theta}(t-1) + P(t)\varphi(t)\varepsilon(t) \tag{42}$$

And finally, according to Eqs. (12) and (16), the parameter-vector and regression variables are defined as follows.

$$\hat{\theta} = [a_1, a_2, b_0, c_1, c_2]$$
$$\varphi^T(t-1) = [-y(t-1), -y(t-2), u(t-2), \varepsilon(t-1), \varepsilon(t-2)] \tag{43}$$

$c_1$ and $c_2$ are coefficients of polynomial $C(q^{-1})$ that presents noise dynamics described in Eq. (16). The conceptual block diagram of the ELS identification method is depicted in Fig.14.
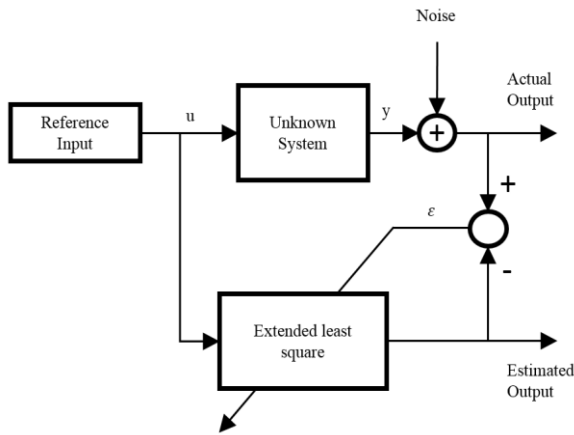


**Fig. 14.** Conceptual block diagram of ELS

# Incremental Minimum Variance Controller

As already mentioned, the minimum variance is just a regulator. In the simplest case, an integrator can be used to solve the tracking problem. The cost function of the IMV controller is the same as the MV regulator. Thus, in this case, we solved the tracking problem with probably high control effort. Fig.15 shows the block diagram of IMVC.
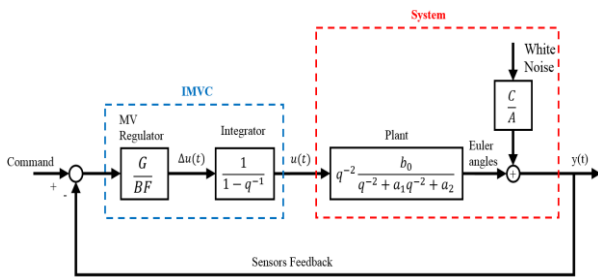


**Fig. 15.** Block diagram of IMVC given in block diagram of Fig. 14

$\Delta u(t)$ can be written as follows.

$$\Delta u(t) = \frac{G}{BF}(r(t) - y(t)) \tag{44}$$

where $r(t)$ is the reference/command input. Assuming that $\Delta$ is defined as $\Delta = 1 - q^{-1}$, Then the control signal is calculated as follows.

$$u(t) = \Delta u(t) + u(t-1) \tag{45}$$

Now, with the presence of $\Delta$, the Diophantine equation will change as below.

$$C = FA\Delta + q^{-d}G \tag{46}$$

where $F$ is a monic polynomial from order $d-1$ and G is from $\max(n_a, n_c - 1)$ degrees proposed as follows.

$$F = 1 + f\_1 q^{\wedge}(-1)$$
$$G = g\_0 + g\_1 q^{\wedge}(-1) + g\_2 q^{\wedge}(-2) \tag{47}$$

By placing the $F$ and $G$ in Eq. 45 we will have $f_1 = c_1 - a_1 + 1$ , $g_0 = c_2 - a_1 f_1 - a_2 + f_1 + a_1$ , $g_1 = a_2 + a_1 f_1 - a_2 f_1$ and $g_2 = a_2 f_1$.

So, the $\Delta u(t)$ is derived as Eq.(48).

$$\Delta u(t) = b_0^{-1}(g_0(r(t) - r(t)) + g_1(r(t-1) - r(t-1)) + g_2(r(t-2) - r(t-2)) - b_0 f_1 \Delta u(t-1)) \tag{48}$$

Finally, the closed-loop system can be shown as Eq. 49.

$$y(t) = \frac{G}{C}r(t-d) + \Delta F e(t) \tag{49}$$

Evidently, $F$ and $G$ polynomials of the IMVC are different from the MV regulator.

So, in each step first $y(t)$ should be calculated from Eq. (49), then $\Delta u(t)$ will be determined from Eq. (44) and finally $u(k)$ will be derived from Eq. (45).

Compared to the MV regulator, the IMVC is suboptimal due to the integrator. It means that the output variance of the system in the presence of the IMV controller is more than the MV regulator case. Indeed, an increase in the system output variance is a penalty (we pay) to achieve the tracking advantage. This is also evident from the mathematical point of view by comparing equations (28) and (49).

**Generalized Minimum Variance Controller**

GMVC is the most complete case of the MV controller class that can be applied to non-minimum phase systems.
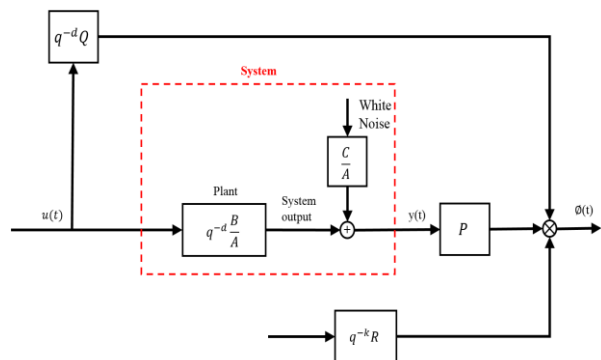
Fig.16 shows the block diagram of the GMVC concept.



**Fig. 16.** Block diagram of GMVC

In figure above, $q^{-d}Q$ is the feed-forward term, which changes the zeroes of the system from the roots of polynomial B to PB + QA. $P$ and $R$ are output and set-point filtering, respectively. It should be noted that $P(0) = 1$.

According to the block diagram of Fig. 14, $\emptyset$ which is called "Generalized Output" is defined as Eq. (50).

$$\emptyset(t + d) = Py(t + d) - Rr(t) + Qu(t) \qquad (50)$$

Eq. (51) is achieved by adding the system equations (Eq. 16) to the generalized output (Eq. 50).

$$\emptyset(t + d) = \frac{PB + QA}{A}u(t) + \frac{PC}{A}e(t + d) \\ - Rr(t) \qquad (51)$$

Additionally, the cost function of this approach is as follows.

$$J = E\{\emptyset^2(t + d)\} \qquad (52)$$

The various limitations of the control signal can be interpreted by $Q$. Indeed, $Q = constant$ is a factor to weighs the loss due to the control action.

As the new cost function suggests, this method focuses on minimizing both output error and control effort.

By multiplying polynomial $E(q^{-1})$ to the system equations (Eq. 16) and some simplifications, $\emptyset$ leads to Eq. (53).

$$\emptyset(t + d) = \frac{1}{C}[(BE + QC)u(t) + Gy(t) - CRr(t)] + Ee(t + d) \qquad (53)$$

The term $Ee(t + d)$ is stochastic and cannot be predicted, consequently, the term in the bracket should be zero for achieving the control goal. Finally, the GMV control signal is calculated as follows.

$$u(t) = F^{-1}(Hr(t) - Gy(t)) \qquad (54)$$

where $H = CR$ and $F = BE + QC$.

The equation of the close-loop system using Eq. (54) and Eq. (16) will be as Eq. (55).

$$y(t) = q^{-d}\frac{BR}{PB + QA}r(t) + \frac{BE + QC}{PB + QA}e(t) \qquad (55)$$

Clearly, the polynomial $(PB + QA)$ should be stable. P and Q help us to place the system's pole to the desired place, and we choose them from orders one and zero, respectively.

As shown in Eq. (56) we selected the polynomial $T(q^{-1})$ with roots in 0.1 and 0.2 as the desired characteristic equation.

$$T(q^{-1}) = z^2 - 0.3z + 0.2 \qquad (56)$$

Format of polynomials $P$ and $Q$ are shown in Eq (57), which are calculated from the Diophantine equation (Eq. 58). The results of the Diophantine equation are shown in Eqs. (59) and (60).

$$P = 1 + p_1 q \quad and \quad Q = \lambda \qquad (57)$$

$$PB + QA = T(q^{-1}) \qquad (58)$$

$$Q = \lambda = \frac{b_0}{0.2 - a_2} \qquad (59)$$

$$p_1 = -\frac{(0.3 - a_1)}{b_0}\lambda \qquad (60)$$

Now, Using the other Diophantine equation (Eq. 63), $G(q^{-1})$ is obtained as a polynomial of order $max(n_a - 1, n_p + n_c - d_0)$ and $E(q^{-1})$ is also a polynomial of order $d_0 - 1$.

$$G(q^{-1}) = g_0 + g_1 q^{-1} \qquad (61)$$

$$E(q^{-1}) = e_0 + e_1 q^{-1} \qquad (62)$$

$$PC = AE + q^{-2}G \qquad (63)$$

Therefore, the unknown parameters will be as follows.

$e_0 = p_0$, $e_1 = p_0 c_1 + 1 - a_1 e_0$, $g_0 = p_0 c_2 + c_1 - a_2 e_0 - a_1 e_1$ and $g_1 = c_2 - a_2 e_1$

In addition, Eq. (64) needs to be established to solve the tracking problem. The result of Eq. (64) is "R", which is shown in Eq. (65).

$$\frac{BR}{PB + QA}\bigg|_{q=1} = 1 \qquad (64)$$

$$R = \frac{\lambda + b_0 p_0 + \lambda a_1 + b_0 + a_2 \lambda}{b_0} \qquad (65)$$

# Simulation

In this section, we are going to demonstrate the preceding theoretical results through numerical simulations.

Specifications of the satellite and the orbit are presented in Table 6.

**Table.6.** Orbit and spacecraft specification

| Parameters | Data |
|---|---|
| **Orbital Elements** | |
| Orbit type | Near Circular |
| Orbit regime | Sun-synchronous |
| Height, h | 660 km |
| Frequency, $\omega_0$ | 0/0011 rad/s |
| Right ascension | 15/7 deg |
| Inclination, i | 98/1 deg |
| Period, T | 98/67 min |
| **Satellite Specification** | |
| mission | Remote sensing |
| Mass, m | 650 kg |
| Moment of inertia, I | diag(1000, 500, 700) |
| Control strategy | 3-axis attitude control |
| **Actuator Datasheet** | |
| mass | < 5 kg |
| Maximum angular rate | 6000 RPM |
| Maximum torque | 0/2 Nm |
| Moment of inertia, $I_w$ | $0/02\ kg.m^2$ |

| Parameters | Data |
|---|---|
| Power Consumption | 18 W |
| Operating Temperature | -5 to +60 C |

The overall simulation block diagram of the attitude control system is shown in Fig.17.

Fig. 18 presents a conceptual relation and interface of ADCS's hardware. On the left-hand side, there are 2 rate gyros(Gyro), 2 magnetometers (MGM), and 3 fine sun sensors(SS). On the right-hand side, there are 3 reaction wheels and 3 orthogonal magnetorquers
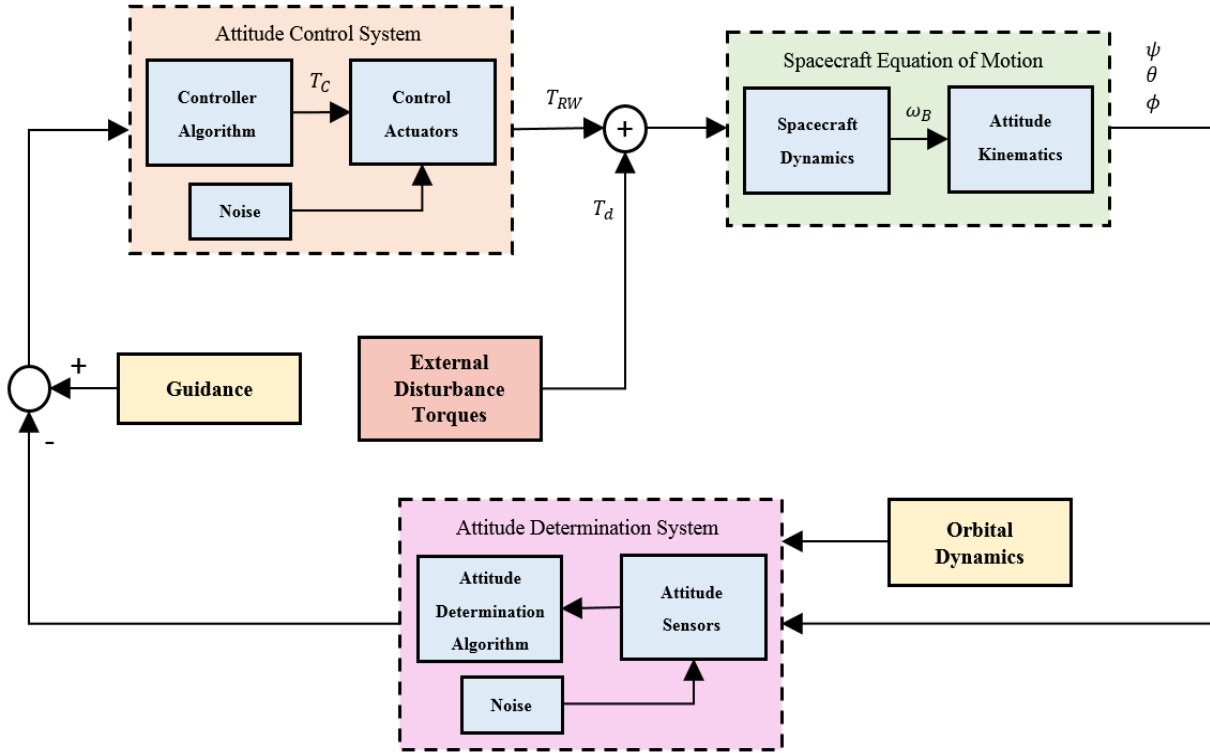


**Fig. 17** Spacecraft Attitude control system block diagram
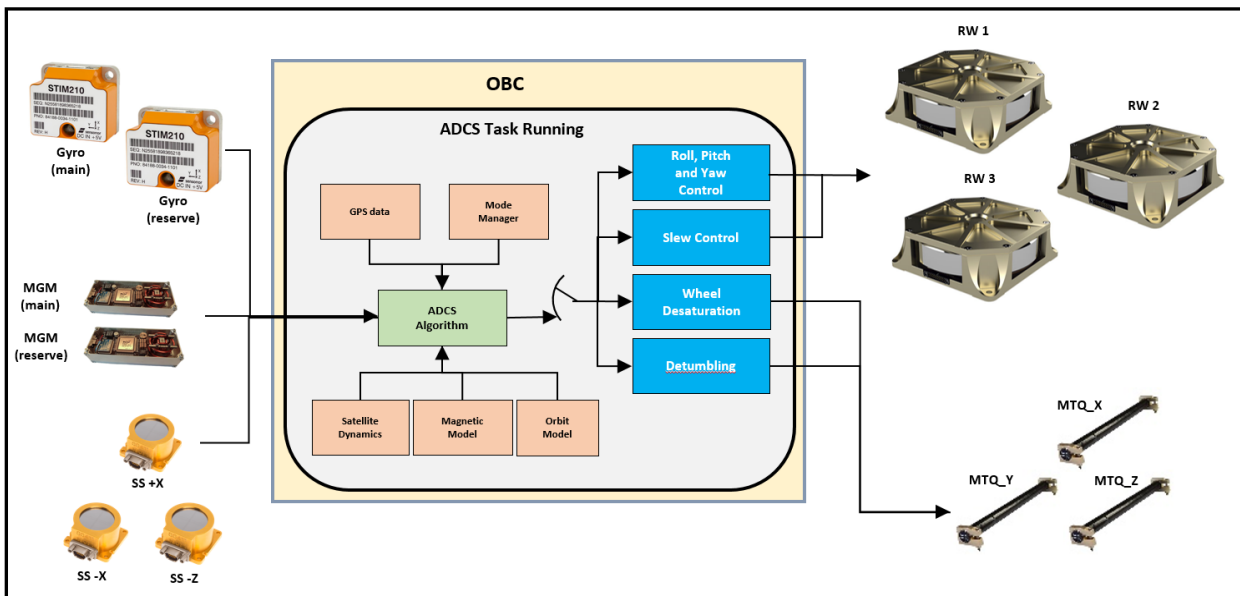


**Fig. 18.** ADCS hardware interface

To evaluate the performance of MV and IMV controllers, we simulated these two controllers based on data in Table 6 and the initial condition of $[\psi_0, \theta_0, \emptyset_0] = [0,0,0]$, $[r_0, q_0, p_0] = [0,0,0]$ and the desired condition of $[\psi_d, \theta_d, \emptyset_d] = [0,0,0]$. Fig. 19 shows the attitude time response of both MV and IMV controllers
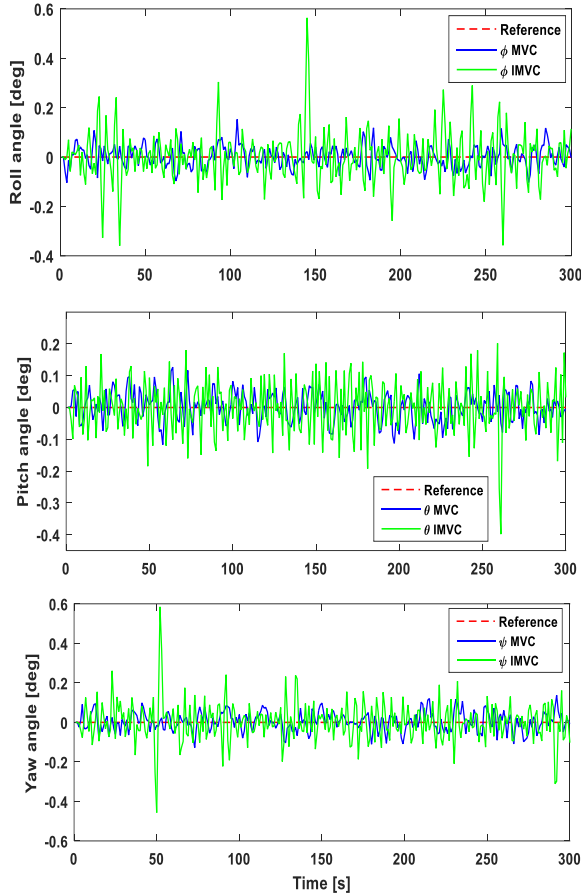


**Fig. 19.** Time response of MV and IMV approach in regulation (zero initial condition)

The Sub-optimality of IMV in comparison with MV regulator is clearly shown in Fig.19, due to its higher output variance. Indeed, IMV is not the best option in the case of regulation goals. Control efforts of MV and IMV controllers are plotted in Fig.20

Predictably, the IMV control effort is greater than the MV control scheme, which makes it a nonsuitable controller for regulation and slow rest-to-rest maneuvers. As mentioned before, IMV approach solves the tracking problem for a higher output variance and control effort (as a penalty).

Fig.20 shows the accumulated loss, also called the "loss function", which is calculated as follows.

$$V(t) = \sum_{i=1}^{T} y^2(i) \qquad (66)$$

The loss function (which is plotted in Fig. 21) is used as the optimality criterion
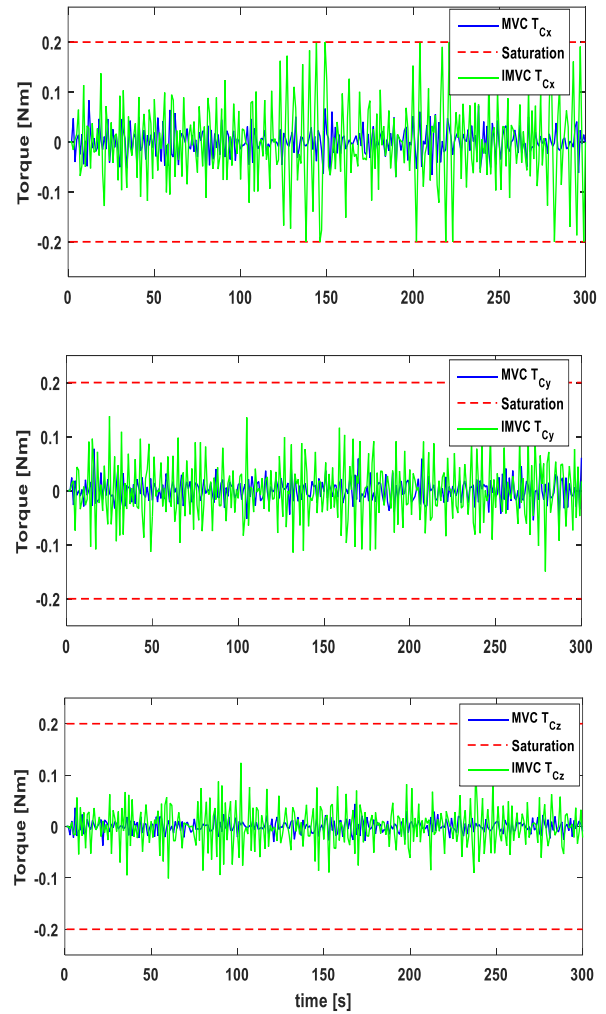


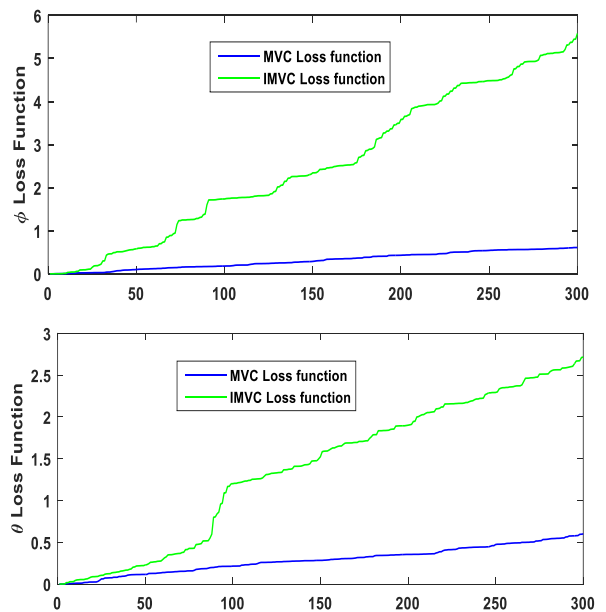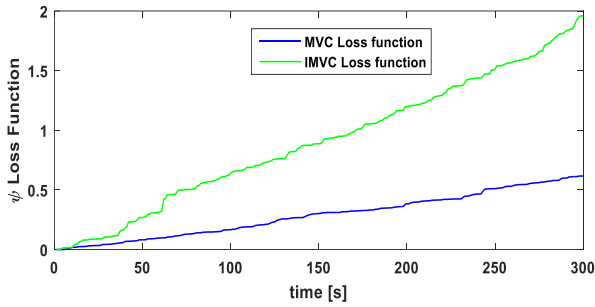**Fig. 20.** Control effort of MV and IMV controller



**Fig. 21.** Loss function of MV and IMV controller

**(Continue) Fig. 21.** Loss function of MV and IMV controller

As we expected, the MV regulator presents the minimum loss function, and the IMV controller is a suboptimal case (in regulation goals) in comparison with the MV regulator. Fig.21 also demonstrates the greater loss of IMV than MV approach.

Table 7 presents the variance of input noise (on the left-hand side column) is affected each channel, and output variance of MV and IMV controller.

**Table. 7.** Desired maneuver specification

| Longitodinal Axis | MV | IMV |
|---|---|---|
| $\text{Var}(e_x(t))=4.2316 \times 10^{-4}$ | $\text{Var}(\phi(t))=21 \times 10^{-4}$ | $\text{Var}(\phi(t))=50 \times 10^{-4}$ |
| **Lateral Axis** | **MV** | **IMV** |
| $\text{Var}(e_y(t))=3.6856 \times 10^{-4}$ | $\text{Var}(\phi(t))=14 \times 10^{-4}$ | $\text{Var}(\phi(t))=64 \times 10^{-4}$ |
| **Directional Axis** | **MV** | **IMV** |
| $\text{Var}(e_z(t))=4.2383 \times 10^{-4}$ | $\text{Var}(\phi(t))=17 \times 10^{-4}$ | $\text{Var}(\phi(t))=59 \times 10^{-4}$ |

As expected, the output variance when using MV regulator is much less than IMV controller. In fact, Table 7 confirms the information of Figure 21 in other words.

Fig.22 shows the time response of the MV regulator and IMV controller in another rest-to-rest maneuver (with the non-zero initial condition). The initial condition is considered as $([\psi, \theta, \phi] = [10, -6, 8])$ and nadir condition is assumed to be the desired condition. Again, the sub-optimality of IMVC compared to the MV approach can be seen in steady-state conditions. In summary, MV approach shows better performance (lower output variance) in regulation goals
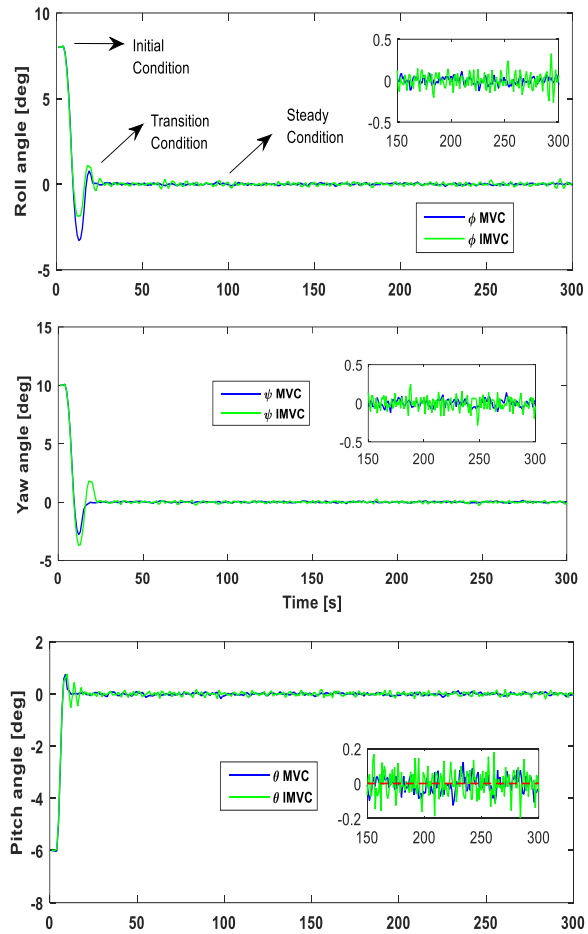


**Fig. 22.** Time response of MC and IMV approach in regulation (non-zero initial condition)

The main Mission Scenario (tri-stereo maneuver) is presented in Fig. 23 and Table 8. In this scenario, ADCS experiences 3 High-precision (HP) modes that refer to the moment of capturing a high-resolution photo. At other times, the ADCS is set on the Low-precision (LP) mode. The initial conditions of this scenario are selected as $[\psi_0, \theta_0, \phi_0] = [6,5,10]$.
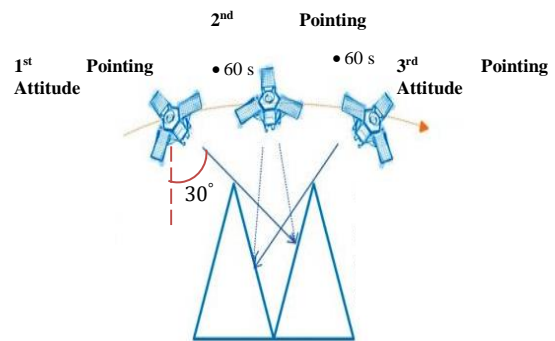


**Fig. 23.** Tri-stereo maneuver scenario

**Table .8.** Desired maneuver specification

| Phase | Attitude $[\phi, \theta, \psi]°$ | Time [s] |
|---|---|---|
| Pre-maneuver | From initial condition of ([6,-5,10]) to nadir ([0,0,0]) pointing. | 60 |
| 1ˢᵗ HP mode | From nadir to first pointing ([−10, −30,0]) attitud. | 60 |
| 2ⁿᵈ HP mode | From first pointing attitude to second ([−10,0,0]) pointing attitude. | 60 |
| 3ʳᵈ HP mode | From second pointing attitude to third ([−10,30,0]) pointing attitude. | 60 |
| Post-maneuver | Return to nadir condition | 60 |

Fig. 24 shows the tracking performance of the MV and IMV controllers. It should be noted that we chose $\lambda = 0.98$ as the forgetting factor.
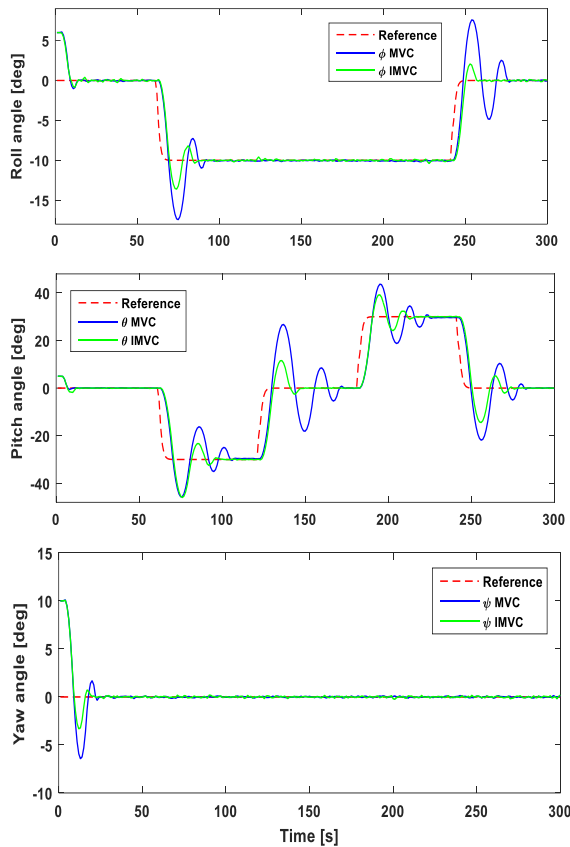


**Fig. 24.** Time response of the MV and IMV controller in providing the tri-stereo imaging scenario

As shown in Fig. 24, IMV presents a more suitable performance and lower settling time in tracking a tri-stereo imaging scenario. In general, IMV approach is more reasonable for tracking problems and we have to accept its suboptimality as a trade-off. Also, Fig. 24 proves that MV approach has no advantages for tracking problems.

The time response of the GMV controller (as a complete approach) is depicted in Fig. 25.

By comparing Figs. 24 and 25, it can be said that the GMV controller provides the most appropriate behavior (short settling-time with minimum overshoot and oscillation). In overall point of view, the GMV controller presents as the best approach to use in a high-resolution remote-sensing satellite control subsystem.

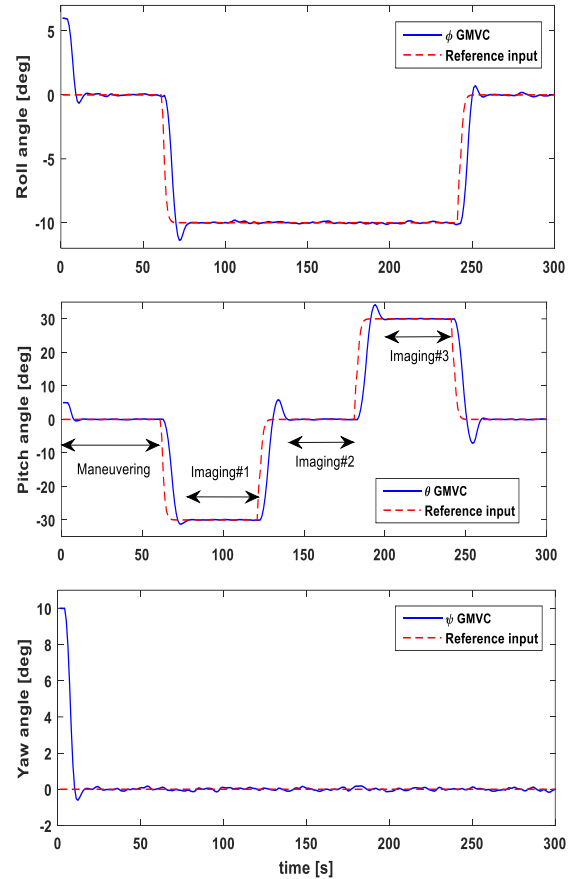The following Fig.26 shows the history of gravity gradient disturbance torque.



**Fig. 25.** Attitude time response of the GMV controller in providing the tri-stereo imaging scenario
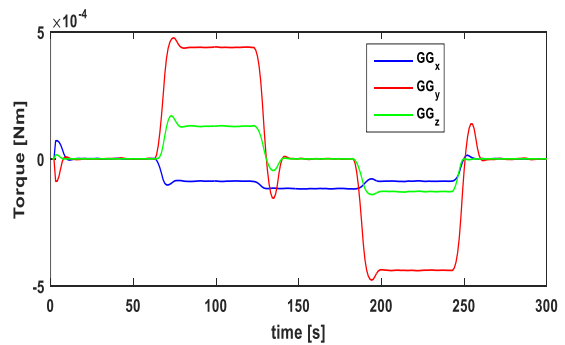


**Fig. 26.** Gravity gradient disturbance torque during imaging phase

Fig.27 shows the control effort of the GMV controller in providing the tri-stereo imaging scenario
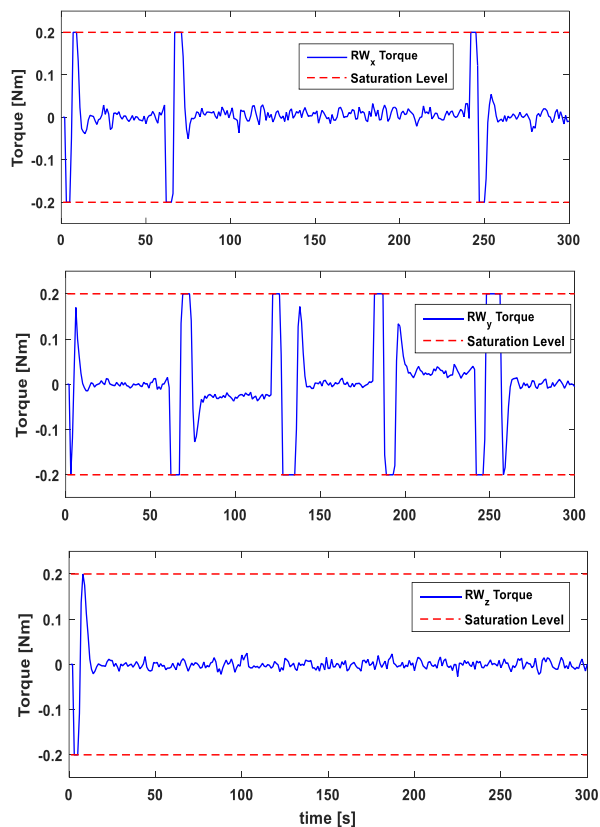
**Fig. 27 .**Control effort of GMV controller

Fig. 27 shows that the control effort sometimes reaches the saturation level ($0.2\,Nm$), which is quite routine for RWs. as mentioned in Section 4-1, in the minimum variance control approach the main goal is to reduce the output variance with any control effort.

Nevertheless, a trade-off can be found between minimizing the output error variance and smoothing control variations, if necessary. By adjusting the suitable weight functions (equation 18), the control effort can be reduced. In this case, the controller is called the "LQG controller".

## Conclusion

The need for optimal control of a system influenced by stochastic disturbances has arisen as a real practical problem in the recent decade. The urgent solution to this problem has primarily been desired by some industrial technologies where the economy, reliability, stability, as well as security of the whole system, depend to a great extent on the performance of the regulation. In recent years, one of the most successful methods for designing optimal control loops that meet these requirements has been the minimum variance control. In our paper, the generalized minimum variance control is considered to control the attitude of asymmetric high-resolution remote sensing satellites. This control scheme has a powerful tool for minimizing the output variance, which is the

most important feature for high-resolution Tri-Stereo-Satellite-Imagery. This approach is especially important when sensors and actuators noise filtering is not possible for any reason.

The simulation results show that for regulation goals, the minimum-variance approach is the best choice. Because it minimizes the output variance as possible as (equal to the white noise variance). For slow and low-angle attitude maneuvers, the IMV controller will present better tracking performance, but greater control effort and output variance. Finally, a Generalized minimum variance controller Recommended as the best control approach due to its smooth, fast, and non-oscillating time-response for both slow and agile maneuvers.

## Conflict of Interests

No conflict of interest has been expressed by the authors.

## Reference

[1].M.Bagnardi, P.J. González, and A. Hooper, "High-resolution digital elevation model from tri-stereo Pleiades-1 satellite imagery for lava flow volume estimates at Fogo Volcano," *Geophysical Research Letters*, Vol.43, No.12, pp. 6267-6275, 2016. https://doi.org/10.1002/2016GL069457

[2] C. Deschamps-Berger, and et al , "Snow depth mapping from stereo satellite imagery in mountainous terrain: evaluation using airborne lidar data," *The Cryosphere Discussions* , Vol. 14, No. 9, pp. 1-28, 2020. doi: https://doi.org/10.5194/tc-14-2925-2020

[3] S. Li et al., "Forest stand height estimation using Ziyuan-3 tri-stereo imagery and Lidar," *in IGARSS IEEE International Geoscience and Remote Sensing Symposium*, pp. 6681-6684, IEEE, 2019. https://doi.org/10.1109/IGARSS.2019.8897913

[4] H. Bolandi, F. F. Saberi, and B. G. Vaghei, "Design of a supervisory adaptive attitude control (SAAC) system for a stereo-imagery satellite based on multiple model control with switching," *International Journal of Innovative Computing, Information and Control*, Vol. 6, No. 9, pp. 4675-4692, 2010.(in Persian)

[5] J. Kim , and et al , "Task Scheduling of Multiple Agile Satellites with Transition Time and Stereo Imaging Constraints," *arXiv preprint* " *arXiv* :1912.00374, 2019. https://doi.org/10.48550/arXiv.1912.00374

[6] A. M. Loghin, J. Otepka, W. Karel, and et al, "Accuracy Analysis of Digital Elevation Models from very High Resolution Satellite Imagery," *Publ. Der DGPF*, Vol. 28, pp. 123-137, 2019.

[7] J. Oh and C. Lee, "Satellite Stereo Image Processing for 3D Topographic Mapping," *Abstracts of the ICA*, Vol. 1, pp. 1-1, 2019. doi: https://doi.org/10.5194/ica-abs-1-276-2019

[8] L. Jian, Z. Yang, and Z. Hefen, "Research on attitude control method of agile satellite based on variable structure control algorithm," *in IGARSS IEEE International Geoscience and Remote Sensing Symposium*, IEEE, pp. 8703-8706, 2019. https://doi.org/10.1109/IGARSS.2019.8898569

[9] J. Kim, J. Ahn, H.-L. Choi, and D.-H. Cho, "Task scheduling of agile satellites with transition time and stereoscopic imaging constraints," *Journal of Aerospace Information Systems*, Vol. 17, No. 6, pp. 285-293, 2020. https://doi.org/10.2514/1.I010775

[10] H. Wang, Z. Yang, Y. Chen, and W. Quan, "A study on the influence of the satellite attitude accuracy on TDICCD imaging," *In 8th IEEE International Symposium on Instrumentation and Control Technology (ISICT) Proceedings,* pp. 219-223, IEEE. 2012. https://doi.org/10.1109/ISICT.2012.6291634

[11] J. R. Wertz, *Spacecraft attitude determination and control* , Springer Science & Business Media. 2012.

[12] A. Kosari, A. Sharifi, A. Ahmadi, and M. Khoshsima, "Remote sensing satellite's attitude control system: rapid performance sizing for passive scan imaging mode," *Aircraft Engineering and Aerospace Technology*, Vol. 92, No. 7, pp. 1073-1083, 2020. (in Persian). https://doi.org/10.1108/AEAT-02-2020-0030

[13] E. A. Hogan and H. Schaub, "Three-axis attitude control using redundant reaction wheels with continuous momentum dumping," *Journal of Guidance, Control, and Dynamics,* Vol. 38, No.10, pp. 1865-1871, 2015. https://doi.org/10.2514/1.G000812

[14] J. Cao, X. Yuan, and Y. Fang, "Tri-Stereo Model Orientation of High-Resolution Satellite Imagery Combining Ground Control Points and Lines," *Photogrammetrie-Fernerkundung-Geoinformation*, pp. 125-140, 2016. https://doi.org/10.1127/pfg/2016/0293

[15] M.S. Siva, "Integrated Relative Position and Attitude Control of Distributed Spacecraft Formation For High Resolution Imaging," PhD diss, 2019.

[16] C. Zhong, Z. Chen, and Y. Guo, "Attitude control for flexible spacecraft with disturbance rejection," *IEEE Transactions on Aerospace and Electronic Systems*, Vol. 53, No. 1, pp. 101-110, 2017. https://doi.org/10.1109/TAES.2017.2649259

[17] Z. Wu, L. Huang, K. Wei, and L. Guo, "Active disturbance rejection control of attitude for spacecraft," *Control Theory and Applications*, Vol. 30, No. 12, pp. 1617-1622, 2013.

[18] A.-F. Lai, Y. Guo, and L.-J. Zheng, "Active disturbance rejection control for spacecraft attitude maneuver and stability," *Control Theory & Applications*, Vol. 29, No. 3, pp. 401-407, 2012. http://dx.doi.org/10.7641/CTA.2013.31034

[19] S. Li, X. Yang, and D. Yang, "Active disturbance rejection control for high pointing accuracy and rotation speed," *Automatica*, Vol. 45, No. 8, pp. 1854-1860,2009. https://doi.org/10.1016/j.automatica.2009.03.029

[20] B. Xiao, Q. Hu, W. Singhose, and X. Huo, "Reaction wheel fault compensation and disturbance rejection for spacecraft attitude tracking," *Journal of Guidance, Control, and Dynamics*, Vol. 36, No. 6, pp. 1565-1575, 2013. http://dx.doi.org/10.2514/1.59839

[21] M. Navabi, S. Soleymanpour, "Command Filtered Modular Adaptive Backstepping Attitude Control of Spacecraft in Presence of Disturbance Torque," *Modares Mechanical Engineering*, Vol. 15, No. 7, pp. 285-296, 2015.(in Persian)

[22] J. R. ODonnell Jr, O. C. Hsu, J. Hanson, and V. Hruby, "The Space Technology 7 disturbance reduction system," in *18th International Symposium on Space Flight Dynamics*. 2004.

[23] J. Ziemer et al., "Colloid microthruster flight performance results from space technology 7 disturbance reduction system," in *International Electric Propulsion Conference (IEPC)* 2017, 2017, No. GSFC-E-DAA-TN47585.

[24] B.Wie, *Space vehicle dynamics and control*, second edition, American Institute of Aeronautics and Astronautics, 2008.

[25] P. W. Fortescue, "Dynamics of spacecraft," *Spacecraft Systems Engineering*, pp. 33-58, 1991.

[26] J. J. Mattice, "Hubble Space Telescope systems engineering case study," The Air Force Institute of Technology (AFIT), 2008. ADA572189

[27] G. Beals, R. Crum, H. Dougherty, and et al, "Hubble Space Telescope precision pointing control system," *Journal of Guidance, Control, and Dynamics*, Vol. 11, No. 2, pp. 119-123, 1988. https://doi.org/10.2514/3.20280

[28] W. Zhou, H. Wang, Z. Ruan, and et al, "High accuracy attitude control system design for satellite with flexible appendages," *Mathematical Problems in Engineering*, Vol. 2014. https://doi.org/10.1155/2014/695758

[29] M.H. Kaplan , *Modern spacecraft dynamics and control*, Courier Dover Publications, 2020.

[30] M. J. Sidi , *Spacecraft dynamics and control*, a practical engineering approach, Vol.7, Cambridge university press, 1997.

[31] K. J. Åström, *Introduction to stochastic control theory*. Courier Corporation, 2012.

[32] D. Simon, *Optimal state estimation: Kalman, H infinity, and nonlinear approaches*. John Wiley & Sons, 2006.

[33] K. J. Åström and B. Wittenmark, *Adaptive control*, Courier Corporation, 2013.

[34] D. Clarke and R. Hastings-James, "Design of digital controllers for randomly disturbed systems," in *Proceedings of the Institution of Electrical Engineers*,

Vol. 118, No. 10: IET, pp. 1503-1506, 1971.doi: 10.1049/piee.1971.0275

[35] D. W. Clarke and P. J. Gawthrop, "Self-tuning controller," in *Proceedings of the Institution of Electrical Engineers*, Vol. 122, No. 9: IET, pp. 929-934, 1975.

[36] H.N. Koivo, "A multivariable self-tuning controller," *Automatica*, Vol.16, No.4, pp. 351-366, 1980. https://doi.org/10.1016/0005-1098(80)90020-5

[37] C. Pukdeboon, A. S. Zinober, and M.-W. L. Thein, "Quasi-continuous higher order sliding-mode controllers for spacecraft-attitude-tracking maneuvers," *IEEE Transactions on Industrial Electronics*, Vol. 57, No. 4, pp. 1436-1444, 2009. http://dx.doi.org/10.1109/TIE.2009.2030215

[38] X. Kong and C. M. Gosselin, "Forward displacement analysis of third-class analytic 3-RPR planar parallel manipulators," *Mechanism and Machine Theory*, Vol. 36, No. 9, pp. 1009-1018, 2001. https://doi.org/10.1016/S0094-114X(01)00038-6

[39] M. Navabi, N. Nasiri, and M. Dehghan, "Modeling and numerical simulation of linear and nonlinear spacecraft attitude dynamics and gravity gradient moments: A comparative study," *Communications in Nonlinear Science and Numerical Simulation*, Vol. 17, No. 2, pp. 1065-1084, 2012. https://doi.org/10.1016/j.cnsns.2011.06.035

[40] B. Sreenivasappa and R. Udaykumar, "Analysis and implementation of discrete time PID controllers using FPGA," *International journal of electrical and computer engineering*, Vol. 2, No. 1, pp. 71-82, 2010.

[41] Y. Okuyama, *Discrete control systems*. Springer, 2014.

[42] "Newspace Systems, NFSS-411 Sun-Sensor Catalogue", [Online] www.newspacesystems.com

[43] "ButterflyGyro, STIM210 multi-axis gyro module Catalogue", [Online] https://www.sensonor.com

[44] B. Wie, *Space vehicle dynamics and control,* Aiaa, 1998.

[45] W. Larson and J. Wertz, "Space mission analysis and design. Torrance, CA (United States); Microcosm," ed: Inc, 1992.

[46] "Newspace Systems, nrwa-t10 reaction wheel Catalogue", [Online] www.newspacesystems.com